



**THERMO-MECHANICAL FATIGUE BEHAVIORS OF
AL-SI 319 AND 356 CAST ALLOYS AND
THE INFLUENCE OF MO ON THEIR EVOLUTION**

PAR

SHUAI WANG

**MÉMOIRE PRÉSENTÉE À L'UNIVERSITÉ DU QUÉBEC À
CHICOUTIMI EN VUE DE L'OBTENTION DU GRADE DE
MAÎTRISEES SCIENCE (M. Sc. A.) EN INGÉNIERIE**

Jury :

X.Grant Chen	Director of research	UQAC	President of Jury
Kun Liu	Codirector of research	UQAC	Internal member
Zhan Zhang	Research Professor	UQAC	Internal member
Emad Elgallad	Research Professor	UQAC	Internal member

QUÉBEC, CANADA

© SHUAI WANG, 2021

RÉSUMÉ

Les alliages coulés Al-Si sont largement utilisés dans l'industrie automobile en raison de leur rapport résistance/poids élevé, de leur bonne coulabilité et de leur recyclabilité. La fatigue thermomécanique (FTM) est l'une des propriétés mécaniques les plus importantes pour évaluer la durée de vie des pièces du moteur avec la charge cyclique et le changement de température. Cependant, il existe une littérature ouverte limitée sur les comportements des FTM dans les alliages coulés Al-Si. D'autre part, à une température de fonctionnement élevée supérieure à 300, le grossissement du précipité entraîne une diminution importante des propriétés mécaniques à température élevée, entraînant des dommages sur le processus de fatigue des alliages coulés Al-Si. Une approche prometteuse pour surmonter ce problème consiste à introduire des dispersoïdes thermiquement stables en alliant des éléments, tels que Mo et Mn. Ainsi, le comportement en fatigue thermomécanique des alliages coulés Al-Si et l'influence de l'ajout de Mo sur leur évolution FTM ont été étudiés dans le présent travail, qui peut être divisé en deux parties.

Dans la première partie de l'enquête, les comportements FTM de deux alliages coulés typiques Al-Si, l'alliage Al-Si-Cu 319 et l'alliage Al-Si-Mg 356, ont été étudiés. Pendant le FTM, les deux alliages peuvent être observés avec un comportement de ramollissement cyclique, tandis que l'alliage 319 présente une contrainte cyclique plus élevée que l'alliage 356. Les résultats montrent que la densité en nombre des précipités de renforcement a considérablement diminué après une exposition prolongée à température élevée, ce qui a entraîné une résistance considérablement réduite. Le taux de grossissement plus élevé du β' - Mg_2Si dans l'alliage 356 a conduit à un taux de ramollissement plus élevé pendant le FTM. Sous traitement thermique de surveillance T7, l'alliage 319 présente une durée de vie en fatigue plus longue que l'alliage 356 dans toutes les amplitudes de déformation testées. Plusieurs modèles de fatigue ont été introduits, et le modèle d'énergie d'hystérésis a été utilisé pour simuler le comportement de la FTM.

Pour la deuxième partie, l'effet de l'ajout de Mo sur les propriétés thermomécaniques des alliages coulés Al-Si a été étudié. Dans les alliages 319 et 356, une quantité substantielle de dispersoïdes α -Al(Fe,Mn,Mo)Si peut être observée dans la matrice avec l'ajout de Mo. Dans l'alliage 319, les dispersoïdes contenant du Mo aident à bloquer le mouvement de la luxation et à maintenir l'effet de renforcement après une longue exposition à des températures élevées. Dans l'alliage 356, la présence de dispersoïdes contenant du Mo thermiquement stables peut homogénéiser la déformation plastique, retarder l'amorçage des fissures et prolonger la durée de vie du FTM. L'alliage 319 présente une résistance à la fatigue plus longue avec l'ajout de Mo dans toutes les amplitudes de déformation testées, et l'alliage 356 présente également une résistance à la fatigue plus longue sous des amplitudes de déformation de 0,4 % et 0,6 %. Le modèle énergétique d'hystérésis a été utilisé pour simuler le comportement FTM de différents alliages et les résultats calculés montrent un bon accord avec les résultats expérimentaux.

ABSTRACT

Al-Si cast alloys are widely used in automobile industries due to their high strength-to-weight ratio, good castability, and recyclability. Thermal-mechanical fatigue (TMF) is one of the most significant mechanical properties to evaluate the service life of engine parts with the cyclic load and temperature change. However, there is limited open literature available on TMF behaviors in Al-Si cast alloys. On the other hand, at high operation temperatures above 300°C, the precipitate coarsening leads to severe decrement on elevated temperature mechanical properties, resulting in damage on fatigue process of Al-Si cast alloys. One promising approach to overcoming this problem is introducing thermally stable dispersoids by alloying elements, such as Mo and Mn. Thus, the thermal-mechanical fatigue behavior of Al-Si cast alloys and the influence of Mo addition on their TMF evolution have been investigated in the present work, which can be divided into two parts.

In the first part of the investigation, the TMF behaviors of two typical Al-Si cast alloys, Al-Si-Cu 319 alloy and Al-Si-Mg 356 alloy, were studied. During TMF, both alloys can be observed with cyclic softening behavior, while 319 alloys show higher cyclic stress than 356 alloys. Results show that the number density of strengthening precipitates significantly decreased after a long time of exposure under elevated temperature, which resulted in a significantly reduced strength. The higher coarsening rate of β' -Mg₂Si in 356 alloys led to a higher softening rate during TMF. Under T7 overaged heat treatment, 319 alloys show longer fatigue life than 356 alloys in all strain amplitudes tested. Several fatigue models have been introduced, and the hysteresis energy model has been used to simulate the TMF behavior.

For the second part, the effect of Mo addition on the thermal-mechanical properties of Al-Si cast alloys has been investigated. In both 319 and 356 alloys, a substantial amount of α -Al(Fe, Mn, Mo)Si dispersoids can be observed in the matrix with Mo addition. In 319 alloy, Mo-containing dispersoids help block the movement of dislocation and maintain the strengthening effect after a long time of exposure under elevated temperature. In 356 alloy, the presence of thermally stable Mo-containing dispersoids can homogenize plastic deformation, delay crack initiation and extend TMF life. 319 alloy shows longer fatigue life with Mo addition in all strain amplitudes tested, and 356 alloy also presents longer fatigue life under 0.4% and 0.6% strain amplitudes. The hysteresis energy model has been used to simulate the TMF behavior of different alloys and the calculated results show a good agreement with the experimental results.

TABLE OF CONTENTS

RÉSUMÉ	ii
ABSTRACT.....	ii
TABLE OF CONTENTS.....	iii
LIST OF TABLE	v
LIST OF FIGURE.....	vi
LIST OF SYMBOLS	ix
ACKNOWLEDGEMENTS	x
CHAPTER 1 INTRODUCTION	11
1.1 Background.....	11
1.2 Objective.....	12
CHAPTER 2 LITERATURE REVIEW	14
2.1 Development of Al-Si cast alloys	14
2.2 Alloying elements in Al-Si cast alloys	15
2.2.1 Silicon.....	15
2.2.2 Magnesium.....	16
2.2.3 Copper	17
2.2.4 Iron	18
2.2.5 Manganese.....	19
2.2.6 Molybdenum	19
2.2.7 Strontium.....	20
2.3 Heat treatment and strengthening mechanism in Al-Si cast alloys.....	21
2.3.1 Solution treatment	21
2.3.2 Quenching	23
2.3.3 Aging treatment.....	24
2.4 Thermo-mechanical fatigue (TMF)	26
2.4.1 Alloying elements.....	29
2.4.2 Casting procedure.....	31
2.4.3 Heat treatment	32
2.4.4 Loading conditions	34

2.5	TMF lifetime characterization and prediction	35
2.6	Summary.....	38
CHAPTER 3	EXPERIMENTAL PROCEDURES.....	39
3.1	Materials	39
3.2	Heat treatment.....	39
3.3	Thermo-mechanical fatigue test	40
3.4	Microstructure characterization	41
3.4.1	Sample preparation.....	41
3.4.2	Optical microscopy.....	42
3.4.3	Scanning electron microscopy.....	42
3.4.4	Transmission electron microscopy	42
CHAPTER 4	THERMO-MECHANICAL FATIGUE PROPERTIES OF AL-SI 319 AND 356 CAST ALLOY	43
4.1	TMF behaviors	43
4.1.1	Cyclic stress-strain behavior.....	43
4.1.2	Lifetime behavior	49
4.1.3	Microstructural observation.....	49
4.2	TMF lifetime parameters	62
4.3	Summary.....	65
CHAPTER 5	EFFECT OF MO ADDITION ON TMF PROPERTIES IN AL-SI CAST ALLOYS	67
5.1	TMF behavior with Mo addition	67
5.1.1	Cyclic stress-strain behavior.....	67
5.1.2	Lifetime behavior	73
5.1.3	Microstructure observation.....	74
5.2	TMF lifetime parameters	84
5.3	Summary.....	86
CHAPTER 6	CONCLUSIONS	88
CHAPTER 7	RECOMMENDATIONS.....	90
REFERENCES	91

LIST OF TABLE

Table 3.1 Chemical composition (wt. %) of experimental alloys	39
Table 3.2. Heat treatment parameters for experimental alloys.	40
Table 4.1 Proportion of stage I in total TMF lifetime of 319 and 356 alloy at different strain amplitudes	48
Table 4.2 Analysis results of microstructure of 319 and 356 alloy before TMF.....	50
Table 4.3 Parameters of precipitates of 319 and 356 alloys	55
Table 4.4 Coarsening rate constant k after various strain amplitude OP-TMF	56
Table 4.5 Value of parameters calculated by the hysteresis energy model	65
Table 5.1 Pre-test time (PT) and initial tensile stress (ITS) of Mo-free and Mo-addition alloys at various strain.	72
Table 5.2 Proportion of stage I in total TMF lifetime of 319 and 356 alloys at a different strain amplitude.....	73
Table 5.3 Analysis results of microstructure of 319 and 356 alloy before TMF.....	75
Table 5.4 Parameters of precipitates of Mo-free and Mo-addition alloys	79
Table 5.5 Parameters of dispersoids of Mo-free and Mo-addition alloys	80
Table 5.6 Coarsening rate constant k of Mo-free and Mo-addition alloys after OP-TMF ...	81
Table 5.7 Value of parameters calculated by hysteresis energy model.	86

LIST OF FIGURE

Figure 2.1 Al-Si phase diagram © 2011 Elsevier B.V. [17].....	15
Figure 2.2 In-phase and Out-of-phase thermo-mechanical loading mode. Reprint with the permission of Taylor & Francis [3].	28
Figure 2.3 Active damage mechanism during an OP-TMF cycle. Reprint with the permission of Taylor & Francis [3]......	28
Figure 3.1 Geometry and dimension of thermo-mechanical fatigue test sample (unit in mm) ©The Minerals, Metals & Materials Society 2019 [113]	41
Figure 4.1 Stress-strain hysteresis loops under OP-TMF loading conditions of 319 and 356 alloy. (a) 319-0.2%, (b) 356-0.2%, (c) 319-0.4%, (d) 356-0.4%, (e) 319-0.6%, and (f) 356-0.6% © Shuai Wang, 2021	45
Figure 4.2 The plastic strain of 319 and 356 alloy under OP-TMF loading at different strain amplitude. © Shuai Wang, 2021	46
Figure 4.3 The evolution of maximum and minimum stress at different strain amplitude for (a)319 alloy and (b) 356 alloy. © Shuai Wang, 2021.....	48
Figure 4.4 Mechanical strain amplitude vs number of cycles for 319 and 356 alloy under OP-TMF loading. © Shuai Wang, 2021.....	49
Figure 4.5 Microstructure before TMF of (a) 319 alloy and (b) 356 alloy. © Shuai Wang, 2021	50
Figure 4.6 The TEM microstructure before TMF of (a) 319-T7 and (b) 356-T7. © Shuai Wang, 2021	51
Figure 4.7 Precipitates microstructure of 319 alloy after TMF, the loading direction is perpendicular to the image, (a) 0.2%, (b) 0.4% and (c) 0.6%.© Shuai Wang, 2021.....	53

Figure 4.8 Precipitates microstructure of 356 alloy after TMF, the loading direction is perpendicular to the image, (a) 0.2%, (b) 0.4% and (c) 0.6%.© Shuai Wang, 2021....	54
Figure 4.9 Crack microstructure after 0.2% TMF test of (a) 319 alloy and (b) 356 alloy. The loading axis is vertical. © Shuai Wang, 2021.....	59
Figure 4.10 Overall view of fracture surface after 0.2% TMF test (a) 319 alloy and (b) 356 alloy. © Shuai Wang, 2021.....	60
Figure 4.11 Fractography and BSE micrograph of fractured specimen after 0.2% TMF test. (a, b) 319 alloy and (c, d) 356 alloy. © Shuai Wang, 2021	61
Figure 4.12 Schematic diagram of hysteresis energy model calculation © 2017 Elsevier B.V. [107].....	62
Figure 4.13 Hysteresis energy as a function of number of cycles for (a) 319 alloy and (b) 356 alloy. © Shuai Wang, 2021	64
Figure 4.14 TMF lifetime results and Hysteresis energy model fitting results for 319 and 356 alloys. © Shuai Wang, 2021	65
Figure 5.1 Stress-strain hysteresis loops under OP-TMF loading conditions of 319 and 319M alloy. (a) 319-0.2%, (b) 319M-0.2%, (c) 319-0.4%, (d) 319M-0.4%, (e) 319-0.6% and (f) 319M-0.6%. © Shuai Wang, 2021.....	68
Figure 5.2 Stress-strain hysteresis loops under OP-TMF loading conditions of 356 and 356M alloy. (a) 356-0.2%, (b) 356M-0.2%, (c) 356-0.4%, (d) 356M-0.4%, (e) 356-0.6% and (f) 356M-0.6%. © Shuai Wang, 2021.....	69
Figure 5.3 The evolution of maximum and minimum stress at different strain amplitude of 319 and 319M alloy, (a) 0.2%, (b) 0.4% and (c) 0.6%.© Shuai Wang, 2021	70
Figure 5.4 The evolution of maximum and minimum stress at different strain amplitude of 356 and 356M alloy, (a) 0.2%, (b) 0.4% and (c) 0.6%.© Shuai Wang, 2021	71

Figure 5.5 Mechanical strain amplitude vs number of cycles of (a) 319/319M alloy, and (b) 356/356M alloy. © Shuai Wang, 2021	73
Figure 5.6 Microstructure before TMF of (a) 319M alloy and (b) 356M alloy. © Shuai Wang, 2021	74
Figure 5.7 TEM microstructure before TMF of (a) 319M alloy and (b) 356M alloy. © Shuai Wang, 2021	76
Figure 5.8 EDS spectrums confirm the composition of dispersoids of 319M and 356M alloys. © Shuai Wang, 2021	76
Figure 5.9 Precipitates microstructure of 319M alloy after TMF, the loading direction is perpendicular to the image, (a) 0.2%, (b) 0.4% and (c) 0.6%.© Shuai Wang, 2021....	77
Figure 5.10 Precipitates microstructure of 356M alloy after TMF, the loading direction is perpendicular to the image, (a) 0.2%, (b) 0.4% and (c) 0.6%.© Shuai Wang, 2021....	78
Figure 5.11 Overall view of fracture surface after 0.2% TMF test (a) 319M alloy and (b) 356M alloy. © Shuai Wang, 2021	82
Figure 5.12 Fractography and BSE micrograph of fractured specimen after 0.2% TMF test. (a, b) 319M alloy and (c, d) 356M alloy. © Shuai Wang, 2021	83
Figure 5.13 Fatigue striations under 4000x magnification in (a) 356-0.4% and (b) 356M-0.4%. © Shuai Wang, 2021	84
Figure 5.14 Hysteresis energy as a function of number of cycles for (a) 319M alloy and (b) 356M alloy. © Shuai Wang, 2021	85
Figure 5.15 TMF lifetime results and hysteresis energy model fitting results for (a) 319 and 319M alloy, (b) 356 and 356M alloy. © Shuai Wang, 2021	86

LIST OF SYMBOLS

α	Thermal expansion coefficient
β	Fatigue damage exponent
C	Shape factor constant
$\Delta\varepsilon_p$	Plastic strain amplitude
$\Delta\sigma$	Stress amplitude
ε_{el}	Elastic strain
ε_{in}	Inelastic strain
ε_{th}	Thermal strain
ε_{tot}	Total strain
ε_{mech}	Mechanical strain
K	Coarsening rate constant
L	Average half-length of precipitates (after TMF)
L_0	Average half-length of precipitates (before TMF)
N_f	TMF lifetime cycles
n	Temporal exponent
T	Test temperature
T_0	Reference temperature
t	Time of TMF test
W_i	Hysteresis energy of the i th cycle
W_s	Saturation hysteresis energy
W_0	Fatigue damage capacity

ACKNOWLEDGEMENTS

First of all, I would like to express my gratefulness and acknowledgment to my supervisor, Dr. X. -Grant Chen, for providing me with the opportunity to study at Université du Québec à Chicoutimi and his support and guidance during my master studies. I would also like to thank Dr. Kun Liu and Dr. Zhan Zhang, for their suggestions and help through my project and thesis and their guidance on my experiment. Thank all my colleagues in CURAL and all the friendly people I meet here at Saguenay, you make my life here more colorful, I'll cherish those days we spent together.

I would like to acknowledge the financial support of the Natural Science and Engineering Research Council of Canada (NSERC) and Rio Tinto Alcan through the NSERC Industry Research Chair in the Metallurgy Aluminum Transformation at Université du Québec à Chicoutimi.

I also want to express my wishes to my best friend Tan, thank you for the chance to be your best man at your wedding. Finally, I would like to express my deepest gratitude to my family, with their encouragement and support I can overcome many challenges and difficulties and finish my master's study.

CHAPTER 1 INTRODUCTION

1.1 Background

Al-Si alloy was increasingly used in the automobile industry for the fabrication of engine components such as engine blocks, cylinder heads, oil pans, and intake manifolds. Al-Si alloy has good castability and thermal conductivity, and is most important for its high strength to weight ratio, making it a suitable substitution of cast iron in engine components fabrication. Nowadays, the development of the automobile industry is driven by the demand to reduce the development times and try to minimize the development costs. On the other hand, climate policy and guidelines were made for reducing greenhouse gas emissions, which makes requirements for motor vehicles [1]. Also, in considering saving fuel and materials, many methods such as downsizing, developing hybrid engines, and automatic start-stop systems are now used in the automobile industry [2]. The start-stop system and downsizing of the engines lead to higher loading, especially the cyclic loading at a wider temperature range. Meanwhile, higher components temperatures and higher ignition pressure is demanded to increase the efficiency of engines. Therefore, all these higher loadings, service temperature, and higher ignition pressure put a higher requirement on materials, especially the mechanical properties at high temperatures.

Thermal-mechanical fatigue is one of the most considerations in industrial design since it is the severe damage occurring during the cyclic loading with temperature change. During TMF, components show inelastic deformation which is driven by a thermal and mechanical strain. There are two major phasing modes, in-phase loading (IP-TMF) and out-of-phase loading (OP-TMF), which are generally applied in the TMF test [3]. There are many researches on TMF behaviors of steel and Ni-based superalloy [4-7], while the open literature on TMF behaviors of Al-Si cast alloys is limited.

Besides, Mo, as one of the dispersoid former elements, is more and more widely introduced into aluminum alloys to improve their elevated temperature properties. For instance, Farkoosh et al. studied the strengthening effect of Mo in Al-7Si-0.5Cu-0.3Mg alloy, the results presented 25% of increased tensile yield strength at 300°C [8], and combined additions of Mo and Mn increased the number of dispersoids, uniformed the distribution, and eliminated the dispersoid free zone (DFZ) [9]. Chen also studied the precipitation behavior of Mo-containing dispersoids and their effects on elevated temperature properties in Al-Si-Mg 356 cast alloy, an optimum aging procedure for precipitation of dispersoid is 520°C/12h or 500°C/4h+540°C/2h, and the presence of Mo dispersoids resulted in a remarkable improvement in the creep resistance with 40% reduction in the minimum creep rate [10]. Though there are many studies focused on Mo. there is little study of Mo on TMF behavior.

Therefore, it is urgent to investigate the TMF behaviors of Al-Si cast alloys and the approaches to improve them to meet the requirement of new demands from modern industries. In the present work, two typical and most often used Al-Si cast alloys, named as Al-Si-Cu 319 and Al-Si-Mg 356 alloys, are selected to understand their TMF behaviors and the response to TMF from Mo addition.

1.2 Objective

Generally, the objective of this project is to investigate the TMF behavior of Al-Si cast alloys and influences on Mo addition the evolution of TMF of these hypoeutectic Al-Si alloy. To achieve the objective, several works will be carried out as follows:

Part I: To study the high-temperature mechanical properties of Al-Si-Cu 319 alloy and Al-Si-Mg 356 alloy with T7 heat treatment by characterizing the cyclic strain-stress evolution, TMF lifetime, microstructure, and fracture morphology with damage mechanisms. TMF tests

were performed under various strain amplitudes (0.2%, 0.4%, 0.6%) and wide temperature range (60°C-300°C). The evolution of precipitates during TMF was quantified for coarsening rate calculation and the hysteresis energy model was used for TMF behavior simulation.

Part II: To evaluate the effect of Mo-containing dispersoid in Al-Si cast alloy by performing TMF test with same strain amplitudes and temperature range. The effect of Mo addition on elevated temperature mechanical properties by discussing the cyclic strain-stress evolution, TMF lifetime, microstructure, and fracture morphology with damage mechanisms. Precipitates quantification and hysteresis energy model was also used for TMF behavior simulation and compared with Mo-free Al-Si alloys.

CHAPTER 2 LITERATURE REVIEW

2.1 Development of Al-Si cast alloys

Compared with iron, steel, and copper, aluminum alloy is well known for its high strength-to-weight ratio, as well as other advantages such as corrosion resistance, good thermal and electric conductivity, and recycling ability. By appropriate alloying and treatment, aluminum alloys are available in a variety of strengths. Besides, aluminum displays excellent machinability and workability, it can be fabricated into various forms such as foil, sheets, rods, tubes, and wires.

Aluminum alloy with silicon as a major alloying element form a class of material that provides a significant part of all casting materials. In recent decades, attributed to economic and environmental requirements of the automotive industry, aluminum alloys were taking increasingly applications in engine components fabrication.

The Al-Si cast alloys which are usually used for engine components can be classified into two main categories: Al-Si-Cu alloys, such as 319, and Al-Si-Mg alloys, such as 356. Aluminum alloys based on 356-type alloy present high ductility and acceptable strength at ambient temperature, but their strength significantly decreases above 200°C [11-14]. The alloys based on 319-type alloy exhibit higher yield and creep strength above 200°C, but show lower ductility [11-14].

2.2 Alloying elements in Al-Si cast alloys

2.2.1 Silicon

Figure 2.1 shows the Al-Si phase diagram, which is the basis of the Al-Si cast alloys [15, 16]. The eutectic point is at 12.5 wt.% Si and a temperature of 577°C. Other alloying elements can affect eutectic Si content, shifting the eutectic point to a higher or lower level.

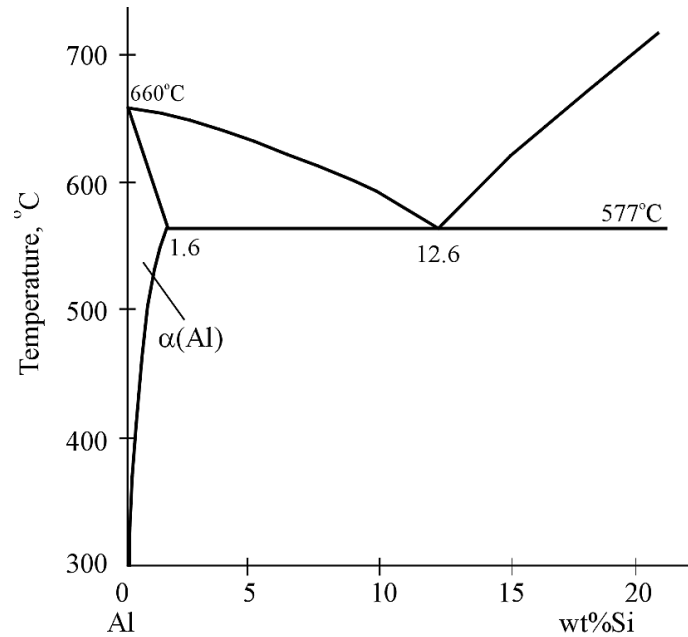


Figure 2.1 Al-Si phase diagram © 2011 Elsevier B.V. [17]

The mechanical properties of Al-Si cast alloys are affected by the amount and morphology of eutectic phases, which are formed during solidification and influenced by alloying elements, cooling rate, and crystallization behavior. The eutectic microstructure can be broadly classified as lamellar, coarse, or refined [18]. The typical Al-Si eutectic morphology is lamellar, which can be ascribed to the low interfacial energy between Al and Si and the strong growth anisotropy of Si [17]. Coarse and lamellar Si particles, which appear under normal solidification conditions, may act as stress concentration sites and crack propagation paths [19-21]. Attribute to the fine structure of the eutectic, the refined microstructure is the

only one considered to have good mechanical properties [22, 23]. Besides, silicon can significantly improve the castability and wear resistance, also contribute to reducing the density and the coefficient of thermal expansion of aluminum alloys.

2.2.2 Magnesium

Magnesium (Mg) is soluble in aluminum up to a maximum of 17.4 wt.% at 450°C. Adding Mg can refine the eutectic Si phase in Al-Si-Cu alloys [19]. Most importantly, Mg is added to Al-7Si cast alloys to induce age hardening through Mg₂Si precipitates, which are coherent with the aluminum matrix. Normally, the Mg content in commercial 356 alloy ranges from 0.3 to 0.4 wt.%. In general, it has been reported that higher Mg content can increase the yield strength, matrix strength, and hardness while decreasing the ductility and fracture toughness [24, 25]. Besides the major effect on the precipitates hardening of Mg, it also depresses the eutectic temperature [26].

In the as-cast microstructure of Al-Si cast alloys, the Mg-containing phases that can form during solidification are Mg₂Si and π -Fe phases. The yield strength increases as the Mg content increases, which is linear up to ~0.6 wt.% of Mg content [27]. π -Fe will transform into β -Fe after solution treatment, but for higher Mg concentration π -Fe phase is stable and may not completely dissolve during solution treatment, which means some Mg are binding with π -Fe and will not able to form precipitates, resulting in dropping in strength.

Based on previous studies, the precipitation sequence during heat treatment in Al-Si-Mg alloy is listed below [28-30]:

Clusters of Si or Mg atoms → dissolution of Mg clusters → formation of Mg/Si co-clusters
→ G.P.-I zones → G.P.-II zones/ β'' precipitates → β' precipitates → β -Mg₂Si precipitates

Precipitation begins with the formation of Guinier Preston (G.P.) zones consisting of enrichment of Mg and Si atoms. Soon, these zones elongate in the [100] direction of the matrix and assume needle-like coherent β'' phase. These needle shape phases grow with time to semi-coherent rods (β' phase) and eventually to platelets non-coherent β -Mg₂Si phase.

2.2.3 Copper

Copper is partially soluble in aluminum solid solution with a maximum solubility of 5.65 wt.%. The addition of Cu in Al-Si cast alloy improves strength, creep resistance, and hardness in the as-cast and heat-treated conditions [31], it also slightly increases the fluidity of alloy and depresses the Si eutectic temperature of ~1.8°C per 1 wt.% Cu added. Cu leads to enhancement of strength in Al-Cu alloy and Al-Si alloy by the formation of hardening precipitates during the heat-treatment process. The Cu content of commercial use 319 alloy ranges from 3 to 4 wt.%.

The major strengthening phase in Al-Si-Cu alloy is the Al₂Cu phase, which has been investigated by many researchers. The precipitation sequence during heat treatment in Al-Cu and Al-Si-Cu alloy is listed below [32-34]:

Supersaturated solid solution → G.P.-I zones → G.P.-II zones/ θ'' precipitates →
 θ' precipitates → θ -Al₂Cu precipitates

Precipitation of the Al_2Cu phase also begins with the formation of G.P. zones of Al and Cu atoms. Then, these zones transform into plate-like θ'' phase, which presents the best enhancement effect. With longer time exposed under elevated temperature, θ'' phase gradually coarsened to θ' phase, and eventually transform into globular θ - Al_2Cu particles.

The plate-shaped morphology of precipitates has a specific orientation relationship with the Al matrix. One is a coherent interface $(001) \theta'' // (001) \alpha\text{-Al}$ on the plate faces, the other one is a semi-coherent interface with $(010) \theta'' // (010) \alpha\text{-Al}$ around the rim of the plates [35-37]. The plate-like morphology of Al_2Cu shows a high aspect ratio of θ'' and θ' plate, which is key to effective strengthening.

2.2.4 Iron

Iron, as the most impurity in Al-Si alloy, can strongly decrease the fluidity and castability. It reduces overall mechanical properties through the formation of brittle intermetallic phases. Fe-bearing intermetallic phases appear in various forms such as $\beta\text{-Al}_5\text{SiFe}$ with platelet morphology, $\alpha\text{-Al-Si-Fe}$, and $\pi\text{-Al}_3\text{FeMg}_3\text{Si}_6$ which appear in the form of Chinese script particles.

Increased Fe level strongly decreases the ductility and tensile strength of Al-Si alloy, while the yield strength remains unaffected. The Fe-bearing compounds are much more likely to fracture under tensile loading conditions compared with Al matrix or modified eutectic Si particles. The detrimental effect of Fe-containing compounds is proportional to their size, volume fraction, and morphology. The size and volume fraction related to Fe content in Al-Si alloy. For different morphology, β -platelets phases are more likely to fracture than α -Fe phases

with Chinese script morphology. Therefore, the formation of α -Fe phases instead of β -Fe phases has a less detrimental effect on the mechanical properties of Al-Si alloy.

2.2.5 Manganese

Manganese is added into Al-Si alloy to help reduce the detrimental effects of Fe, which is difficult to eliminate in Al-Si alloy. It has been reported that with a Fe/Mn ratio of 2:1 can be sufficiently substituted β -Al₅FeSi phase into α -Al₁₅(Fe, Mn)₃Si₂ phase [38-40], which improves the mechanical properties of Al-Si alloy. However, some researchers stated that even at these levels of Mn contents some β -Fe phase still can form during heat treatment. Some recent research reported that the combined addition of Mn and other elements such as Cr, Co, or Mo can modify the β -Fe phase more efficiently and improve tensile properties [41-44].

2.2.6 Molybdenum

Mo in aluminum was found can potentially form a large number of dispersoids in Al-Si cast alloy even added at a low level. The low diffusivity of Mo in Al ($2.3 \times 10^{-26} \text{ m}^2\text{s}^{-1}$ at 300°C) along with the limited solid solubility ($\sim 0.25 \text{ wt.}\%$ at peritectic temperature, 660°C), which decrease rapidly with decreasing temperature, makes it a high possibility to form dispersoid that can effectively pin the dislocations in the dendrite grain interiors and improve the mechanical properties. With Mo addition, a substantial amount of nano-scale Al(Fe, Mo)Si dispersoids precipitated during the solid solution process in Al-Si cast alloy, which was thermally stable after longtime exposure under elevated temperature and retained their strengthening effect [8].

As described above, Mo addition in Al-Si cast alloy forms coherent Al(Fe, Mo)Si dispersoids, which are mostly located within interdendritic regions. While the combination of

Mo and Mn can form a large volume fraction of uniformly distributed dispersoids in the Al matrix, due to the opposite partitioning behavior during non-equilibrium solidification ($k_{Mo}>1$ vs. $k_{Mn}<1$). The addition of Mn increases the number of dispersoids by substituting Fe atoms. The combined addition of Mn and Mo leads to a uniform dispersoids distribution by eliminating the interdendritic dispersoid free zones [9].

Many researchers investigated Mo addition in aluminum alloys. Farkoosh et al. studied Mo addition in Al-7Si-0.5Cu-0.3Mg (wt.%) alloy. They reported the tensile yield stress of modified alloy increased 25% at 300°C, which attribute to the formation of Al-(Fe, Mo)-Si dispersoids. It also found Mo addition suppressed the formation of brittle plate-like β -Al₅FeSi and formed a blocky intermetallic phase, which resulted in a 34% increase in elongation at 300°C [8]. Similar results were also reported by Shaha and Jin [43, 45, 46]. Zamani investigated the role of Mo addition on the mechanical properties of Al-Si-Cu-Mg alloy in as-cast and heat-treated conditions at ambient and elevated temperatures, it reported yield strength and hardness remain unaffected by Mo addition at ambient and elevated temperature, and too much presence of Mo may deteriorate the tensile strength at room temperature [47].

2.2.7 Strontium

Strontium is a very effective element to change the size, amount, and morphology of intermetallic compounds. Sr influences Si morphology by changing it from acicular to lamellar or fibrous [48]. There is no consensus in the literature regarding the Sr level to achieve the desired degree of eutectic Si modification in different alloys. The Sr amount for modification has been suggested from 50 to 600 ppm. This wide range can be attributed to variations in melt chemistries, treatment methods, and solidification rates. Besides changing the eutectic Si morphology, Sr also modifies the type of Cu phases.

2.3 Heat treatment and strengthening mechanism in Al-Si cast alloys

Al-Si cast alloys for commercial use normally accompany different kinds of demands on mechanical properties for various applications. However, the mechanical properties of Al-Si cast alloys under as-cast conditions are depended on the composition and the casting procedure. To meet the different demands of mechanical properties. Various heat treatment methods, combined with different temperatures and times are carried out. The heat treatment processes are involved three stages: solution treatment, quenching, and aging treatment.

For common heat treatment applied for Al-Si cast alloy, two major kinds of heat treatment are used. One is the age hardening of the as-cast alloy (T5 treatment) and the age-hardening after solution treatment (T6, T7 treatment) [49, 50]. The T5 heat treatment is performed under the condition that the peak mechanical properties are not required, this helps reduce the production cost as the solution treatment is not performed. T6 (peak aged) and T7 (over-aged) heat treatment are the most common heat treatment method used for Al-Si cast alloy. The T6 heat treatment is normally used for applications under room temperature, while the T7 heat treatment is used for elevated temperature applications [51-53].

2.3.1 Solution treatment

The solution treatment is performed at a high temperature which is close to the eutectic temperature of the alloy. The objective for solution heat treatments is (1) to dissolve Cu and/or Mg-containing constituents into solid solution; (2) to homogenize the alloying elements for precipitation hardening; (3) to spheroid the eutectic Si particles and improve the ductility of the alloy. The dissolution rate of intermetallic phases is highly related to the temperature of solution treatment. However, the maximum solution treatment temperature is limited by

possible incipient melting of the last solidified phase [54-56]. Incipient melting extremely decreases the mechanical properties as a result of void formation.

Cast Al-Si-Mg alloys can be solution treated at 540-550°C, while for Al-Si-Cu alloys which have Cu-containing phases start melting at 505°C [57]. According to previous research, β -Mg₂Si and θ -Al₂Cu phases are easy to dissolve, while other phases such as Q-Al₅Mg₈Cu₂Si₆ particles are relatively hard to dissolve [54]. Phases which contain Fe are hard to dissolve, the α -Al₁₅(Fe, Mn)₃Si₂ phase with Chinese script morphology is almost unaffected by solution treatment, while the brittle β -Al₅FeSi platelet fragments gradually dissolve after long time exposure under elevated temperature [58]. The atoms which not dissolved into the Al matrix during solution treatment are not available for precipitation hardening after aging treatment.

Atoms detach from the intermetallic particles during solidification, they diffuse through the matrix and as results decrease the level of element concentration, and a homogeneous solid solution is formed. The homogenization time is determined by the nature of diffusion atoms and diffusion rate which is related to the temperature of solution treatment. Besides, the diffusion distance which is determined by the coarseness of the microstructure also affects the homogenization behavior during solidification [56].

As discussed previously, the eutectic Si phase has a great influence on mechanical properties. Casting methods and chemical modification help Si particles which with lamellar or acicular morphology much easier to fragment and spheroid during solution treatment [59]. The spheroidization time of eutectic Si particles is mainly affected by solution temperature and the initial size of Si particles.

Due to the risk of incipient melting, the alloy containing Cu phases cannot be solution treated at a high temperature as the alloy only contains Mg phases. However, solution treatment at a relatively lower temperature may not fulfill the purpose of solid solution treatment as the alloying elements and vacancies are not completely dissolved or have less spheroidization level eutectic Si particles. To reach the desired solid solution level of alloying elements, some researchers investigated and suggested the possibility of using a two-stage solution treatment. Sokolowski et al. investigated the solution treatment difference of Al-7Si-3.7Cu-0.23Mg alloy [60, 61], it reported that single-step solution treatment of this alloy must be less than 495°C, is neither able to maximize the dissolution of Cu rich phases nor able to homogenize the microstructure and modify the eutectic Si particles. They proposed a two-step solution treatment, in which the alloy is first solution treated 8h at 495°C then followed by 2h treatment at 520°C. During the first step of the solution treatment, the Cu-containing phases with the lowest melting point would be dissolved, then the following step with higher solution temperature could dissolve the remaining Cu-containing phase and further homogenize the microstructure [62]. This procedure resulted in an increment in both strength and ductility.

2.3.2 Quenching

The purpose of quenching is to maintain the solid solution and prevent element diffusion by rapidly cooling the alloy to a low temperature. During quenching, solute atoms and vacancies are frozen in the Al matrix. These concentrations of solute atoms have a higher level than equilibrium conditions, resulting in a supersaturated solid solution with unstable thermal stability [56, 63].

The precipitation kinetics mainly depends on the degree of supersaturated solid solution and the diffusion rate, which are inversely proportional to the temperature. For most

aluminum alloys, the maximum nucleation and growth rates of precipitates occur under a temperature range of 200°C to 450°C. To prevent premature precipitation, the time spent in this temperature region should be very short, which means less possibility the precipitation occurs during the quenching process. Water is a commonly used quenching media that can provide a high cooling rate to form a supersaturated solid solution.

2.3.3 Aging treatment

Aging treatment takes place at room temperature (natural aging) or an elevated temperature range of 150°C to 210°C (artificial aging), to form uniformly distributed small precipitates which provide high strength of the alloy. Time and temperature are two main factors that affect the strengthening behavior, with higher aging temperature, the aging process is accelerated by increasing nucleation and growth rates.

As discussed above, the precipitate process follows the precipitation sequence during aging treatment. Precipitation begins with the formation of the G.P. zones, then metastable precipitates, either coherent or semi-coherent, form in the Al matrix [64, 65]. Precipitates may nucleate on the G.P. zones if they reached a critical size, or homogeneously in the matrix, or heterogeneously on dislocations or other lattice defects. The metastable precipitates grow by diffusion of alloying elements from supersaturated solid solution to the precipitates during the aging process. Precipitates continue growth by Ostwald ripening, as the supersaturation level decreases. The Ostwald ripening is driven by the reduction of surface energy, resulting in the larger precipitates coarsen as the smaller precipitates dissolve [66]. As the precipitates grow, the coherency strain increase, when the interfacial bond strength is exceeded, precipitates become non-coherent to the matrix, which is also the equilibrium phase that forms by the end

of the precipitation sequence. However, depending on the thermal history of the material, the precipitation may not follow the above sequence and start from an intermediate stage.

The precipitation hardening produces fine particles based on changes in solid solubility with temperature. These particles harden the material by restricting the movement of dislocations in the lattice since dislocations are considered as dominant plasticity carrier of the material. The strength is determined by the size and distribution of precipitates and the coherency of precipitates with the matrix. The precipitates forms in the early aging stage are small and coherent, it can be relatively easily cut by dislocations. As the phase approaches equilibrium during aging treatment, precipitates grow larger due to the Ostwald ripening and the interspace between particles also increased. Hence, the dislocations are not cut the precipitates but have to bypass them by the Orowan mechanism [66].

Precipitates with small size and interspacing lead to a maximum yield strength when dislocations shear through them, it causes a low level of local work hardening and the plastic deformation is restricted on few active slip planes, which is probably deleterious to the fatigue behavior. For large size and interspacing of precipitates, dislocation bypassing results in rapid work hardening, and the plastic deformation is distributed throughout the material, while the yield strength is not high enough as the weak strengthening effect provided by these precipitates. Fine stated that the interesting possibility is to have a dispersion of two kinds of second phase particles, small closely spaced particles to give high yield strength together with large particles to distribute plastic deformation throughout the material [67]. The peak strengthening T6 treatment and the over-aged T7 treatment is widely used for aluminum alloys. The T6 treatment with metastable microstructure involves both coherent and semi-coherent particles, which provide the best strengthening effect. While for T7 treatment, with higher treatment temperatures and longer treatment times, precipitates are more coarsen and less

coherent, resulting in materials with T7 treatment showing a slight decrement in strength but increment on ductility over the T6 treatment.

Besides the precipitation hardening which is described above, dispersoid hardening is also a major strengthening method used for cast Al alloys. Dispersoid refers to precipitates formed with transition elements that have good thermal stability. Precipitation hardening improves the strength of cast Al-alloys while the metastable precipitates dissolve/coarsened at elevated temperature, resulting in softening of the material, which is one major problem for precipitation hardened Al alloys. Dispersoids which are thermodynamically stable together with low solid solubility, as well as limited diffusivity of the solute in Al, are essential for high strength, high-temperature Al alloys. Strength increment by dispersoid hardening depends on the particle size, distribution, and interparticle spacing. Therefore, dispersoids with fine size and are closely-spaced are more effective for dispersoid hardening.

2.4 Thermo-mechanical fatigue (TMF)

As far as the engine components are concerned, a complex loading is applied to those components. Except for the mechanical loading applied to engine components during engine working, a thermal gradient between the combustion chamber and the cooling system results in thermal loading applied to engine components. The thermo-mechanical cyclic loading leads to fatigue failure on these components as the automobile works. Depending on the thermal loading condition, it can be identified as low-cycle fatigue (LCF) which is subject to a constant temperature, and thermo-mechanical fatigue (TMF) which is subject to cyclic temperature.

Different from High-cycle fatigue (HCF), which is subject to constant temperature with loadings that result in purely elastic strains, both LCF and TMF show inelastic deformation on components, which is considered driven by thermal and mechanical strain during engine

working. To assess the lifetime of engine components, LCF and TMF tests under strain control are held for different materials. As the LCF tests are held under constant temperature, the strain rate is decoupled with temperature. However, for the TMF tests, as held under cyclic temperature, the strain rate is dependent on the heating and cooling rates [68]. TMF tests are widely accepted for better simulating the real condition of engine components than other tests.

In TMF tests, as the material under the thermo-mechanical loading condition, the total strain (ϵ_{tot}) is the sum of thermal strain (ϵ_{th}) and mechanical strain (ϵ_{mech}), the latter is composed of elastic strain (ϵ_{el}) and inelastic strain (ϵ_{in}), as Equation 1 shown below [3]:

$$\epsilon_{tot} = \epsilon_{th} + \epsilon_{mech} = a(T - T_0) + \epsilon_{el} + \epsilon_{in} \quad \text{Equation 1}$$

where a is the thermal expansion coefficient, T_0 is the reference temperature, and T is the test temperature.

Besides, during TMF, the thermal and mechanical strain may apply to specimens in different phasing [69, 70]. There is two major phasing mode which generally applied in the TMF test. One stands for in-phase loading, where the maximum mechanical strain occurs at the maximum temperature, the other is out-of-phase loading, where the maximum mechanical strain occurs at the minimum temperature. Some researchers also investigated TMF behavior with phase angles which are different from IP-TMF and OP-TMF [6, 71]. Variations of strain with time corresponding to IP-TMF and OP-TMF loading are illustrated in Figure 2.2 [3].

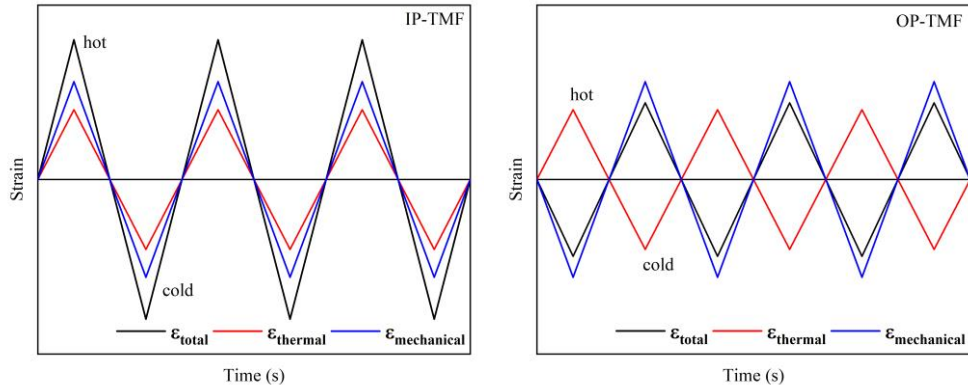


Figure 2.2 In-phase and Out-of-phase thermo-mechanical loading mode.

Reprint with the permission of Taylor & Francis [3].

It has been reported that the governing damage which occurred in engine components is OP-TMF loading [72, 73]. In each cycle of OP-TMF, as the specimen crosses a temperature range, several thermal-activated processes can affect the specimen, as shown in Figure 2.3. The major damage mechanisms of TMF are fatigue, creep, and environment (oxidation) [4, 74]. These damage mechanisms can affect the specimen individually or have interactions mutually. For OP-TMF loading, fatigue and oxidation damage mechanism are more likely to occur during the test.

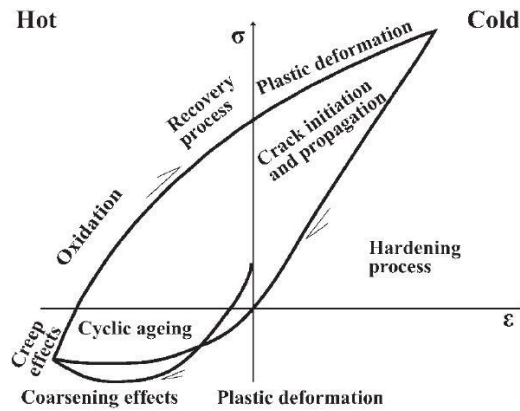


Figure 2.3 Active damage mechanism during an OP-TMF cycle.

Reprint with the permission of Taylor & Francis [3].

During the start-stop cycle of the engine, the repetition of compression-tensile stress cycles is considered to cause cracking in these components, which makes the number of engine start-stop cycles a better indicator of TMF failure [11, 73]. The fatigue failure process can be divided into crack initiation and crack propagation. The amount of crack initiation is dependent on the definition of a crack and also if the material is defect-free or contains large imperfections [4, 75]. To prevent crack initiation, the alloy for engine components needs to have either high yield strength to accommodate stress elastically, or high ductility to delay crack formation [12, 76, 77]. TMF resistance can be improved by many parameters such as high thermal conductivity, low thermal expansion coefficient, microstructural stability, low porosity level, and low content of intermetallic phases, which can be achieved by heat treatment, casting procedure, and alloying elements. The following paragraphs provide an overview of the current TMF research and discussed the factors which influence TMF behavior and lifetime.

2.4.1 Alloying elements

Sehitoglu et al. investigated the TMF behavior of A319 alloy with different Fe contents [78]. The results showed higher stress levels for lower Fe contents and more rapid softening behavior for higher Fe levels.

Huter et al. performed ambient condition fatigue investigation with different types of Al-Si-Cu and Al-Si-Mg cast alloy with varying Si, Cu, Fe, and Sr contents in HCF and LCF loading conditions. The observation results showed that the crack propagation speed and the crack paths were majorly influenced by the eutectic Si. Besides, the precipitation hardening due to Cu significantly affected the fatigue endurance. For high plasticity, the influence of Si is almost lost and only the matrix strength is crucial, the increased fatigue strength in high loaded LCF was observed for alloys with less Cu content which show higher ductility. By

contrast, the improved HCF and low-loaded LCF endurance were only achieved when the matrix strength was increased by precipitation hardening of Cu content. As the crack nucleation mainly occurred on Si particles, Sr as a refinement agent influenced the early crack onset and accordingly the fatigue in total [79]. Later they tested different hypoeutectic Al-Si cast alloys with varying Si, Cu, and Fe contents under TMF. Their results underlined the hard phases act as an important role for crack nucleation, which got ruptured during TMF and independent of the applied mechanical loading, especially in high copper content alloys. In contrast, damages in low copper content alloys were caused by high plastic matrix deformations and the loss of adhesion of eutectic Si particles. They also mentioned the detrimental effect of Fe content on fatigue endurance [80].

Moizumi investigated the mechanical properties of AC4C cast aluminum alloy with different Mg and Cu content under T7 heat treatment and OP-TMF loading conditions concluded that excessive Cu addition in Al-Si-Mg alloy can increase the thermal fatigue life [81]. They also researched the relationship between age-hardening and thermo-mechanical fatigue life in Al-Si-Mg-Cu cast alloys. The age-hardening behavior of the alloys is almost similar for Cu-free and Cu-containing alloys up to the peak aging, while the softening behavior of over aging condition is different depending on Cu contents. The Q' and Q phase is formed in the alloys with higher Cu contents and retards the hardness decrease during over aging and the decrease in the loop-edge stress during the initial stage of thermo-mechanical fatigue cycles [82].

Firouzdor et al studied the effect of microstructural constituents on the thermal fatigue resistance of A319 aluminum casting alloy, which the thermo-mechanical fatigue tests were performed under a thermal range of 40 and 250°C. Results showed that samples with finer

SDAS, lower porosity level, and lower brittle intermetallic contents, as well as higher Si modification, showed better thermal resistance [76].

Shower compared the high-temperature compressive response of 319 and RR350 cast aluminum alloys. By the microstructure observation results, the effectiveness of precipitation strengthening decreases with prolonged exposure to a temperature above 200°C, which the coarsening behavior of theta phase leads to a decrease in strengthening [83]. Roy also compared the effect of strengthening precipitates on the mechanical response for different cast aluminum alloy systems (Al-Cu, Al-Si-Cu, Al-Si, and Al-Si-Mg), with observation and quantification of nano-scale strengthening precipitates, they concluded that alloy with a microstructure that compromises between thermal and mechanical properties will lead to the highest performance [84].

Later Shower et al studied the thermal stability of θ' microstructure of Al-Cu alloy. By phase-field simulation, they proposed a critical θ' aspect ratio criterion to predict the onset of detrimental θ' to θ transformation, and the mobility of Cu in the θ' microstructure was shown to be the dominant factor in determining its morphological stability at elevated temperature [85].

2.4.2 Casting procedure

Sehitoglu et al researched the stress-strain behavior of cast 319-T6 alloys with different SDAS under OP-TMF loading conditions [86]. Results showed that the rapidly solidified material with small SDAS displayed the highest cyclic stress-strain amplitudes, and the stress levels decrease gradually as the SDAS levels increase.

Wang et al studied the influence of casting defects on room temperature fatigue performance of Sr-modified A356-T6 alloy [87]. Results showed that casting with defects shows at least an order of magnitude lower fatigue life than defect-free ones. The decrease in fatigue life is directly correlated to the increase of defect size. It also mentioned that porosity is more detrimental to fatigue life than oxidation damage.

2.4.3 Heat treatment

Moizumi et al examined the thermal fatigue behavior of A356+1% Cu alloy under peak-aged and over-aged conditions [88]. The thermal fatigue life of the over-aged specimen was two times longer than that of the peak-aged specimen, which related to the predominant crack propagation path provided by fractured eutectic Si particles during the thermal fatigue test.

Moverare performed an OP-TMF test on CMSX-4 cast single-crystal nickel-base superalloy under virgin and aged conditions [89]. Though the OP-TMF response was found to be very similar in virgin and aged conditions, a more ductile fracture was found for aged material.

Chan et al studied the effect of heat-treatment on the fatigue crack growth and fracture paths in B319 and A356 cast aluminum alloy. Results showed that the fatigue processes are dependent on microstructure, for B319-T5 and B319-T6, the fatigue processes involved cracking of eutectic Si and intermetallic particles ahead of the crack-tip and localized shear failure in the matrix, while fatigue cracks propagated mostly in the Al-matrix with only small amounts of interaction with the particles in the T7 condition, the fatigue process in A356-T6 is dominated by decohesion of particle/matrix interface. The fracture toughness of A356-T6 is

higher than those B319 alloy in T5, T6, and T7 conditions, the higher fracture toughness exhibited by A356-T6 contributes to the microstructure which contains a more ductile matrix that exhibits uniform plastic flow without the formation of localized shear bands in the matrix [90].

Azadi et al studied the TMF behavior of heat-treated and un-heat treated A356 aluminum alloy. Results showed that the heat treatment has no significant effect on A356 alloy under TMF loadings. By increasing the temperature range, the difference in fatigue lifetime between A356 and A356-T6 decreases. The amount of cyclic softening in A356-T6 alloy is more than A356, the plastic strain increases severely during the TMF lifetime of A356-T6 alloy due to the over-aging phenomenon [91].

Nandy examined the LCF performance of AA6063 Al-Mg-Si alloy with under-aged, peak-aged, and over-aged heat treatment conditions. The under-aged samples exhibit cyclic hardening at strain amplitudes greater than 0.4% which is due to the dynamic precipitation. The peak-aged and over-aged states show hardening only for a few cycles then followed by prolonged cyclic softening. The softening behavior in peak-aged samples is due to shearing of precipitates while that in over-aged samples owing to the reversibility of slip by the formation and annihilation of the Orowan loops around the β -Mg₂Si precipitates [92].

Chen investigated the evolution of dispersoid influenced by adding Mo to Al-Si-Mg alloy during various heat treatments. Results showed that Mo greatly promoted the formation of a-dispersoids. The solution treatment of 520°C/12h or 500°C/4h+540°C/2h was found as the optimum condition for dispersoids, leading to the highest difference between Mo containing alloy and the base alloy. The tensile strengths were improved at both room temperature and elevated temperature [10].

2.4.4 Loading conditions

Toyoda et al investigated the microstructural change of Al-Si-Cu-Mg cast alloy under thermo-mechanical cyclic loading conditions. Although the out-of-phase thermo-mechanical fatigue loading was applied after the alloy was tempered to the T6 peak aging condition, preferential orientation of precipitates is observed together with anisotropy in deformation behavior. The precipitates are observed to align perpendicular to compressive stress during heating, which contributes to the existence of a large negative misfit (~4.5%) in the perpendicular direction relative to the plate surface of the theta phase during the stress-aging process [93]. Toda studied the effect of preliminary thermomechanical treatments (PTMT) for age-hardening aluminum alloys on TMF resistance. Preferential precipitates orientation of perpendicular to the loading direction, achieved by applying OP-PTMT with small temperature and strain ranges, can prolong IP-TMF life effectively [94].

Beck performed OP-TMF tests with superimposed HCF loading on three casts Al-Si alloys, all materials show the number of TMF cycles to failure is not significantly affected by the superimposed HCF loading as the amplitude of the superimposed HCF loading is below a threshold, and above this threshold, the TMF life shows a strong decrease with increasing superimposed HCF loading. The damage processes show that the cyclic deformation and crack initiation are mainly governed by the TMF cycles which induce large plastic deformations, the peak stress and the plastic strain amplitude determine the number of cycles to the crack initiation. The superimposed HCF loading, due to its small amplitude and high frequency, has no significant influence on the first stage of damage, while for crack propagation, even the strain amplitude is very small, also resulting in a strong increase of crack propagation rate [95]. Further research also found that the case when HCF loading is only superimposed tensile stresses are induced in the specimen during the TMF cycle can significantly affect the crack propagation behavior [96].

Han et al researched the TMF behavior in an $\langle 001 \rangle$ oriented nickel-based single crystal superalloy under different cycles of strain and temperature. Results showed that IP-TMF lifetime is longer than those of OP-TMF, and the maximum tensile stress level was concluded to be the lifetime-limiting factor. Cracks were found to initiate from the specimen surface and propagate inwardly during TMF tests, creep and oxidation is the dominant damage mechanism in IP-TMF and OP-TMF, respectively [7].

Neu et al performed both IP-TMF and OP-TMF on 1070 steel specimens in air and helium atmospheres. Results showed that the fatigue life is 2 to 12 times higher in helium than in air, indicating that oxidation-induced crack nucleation and crack propagation are detrimental for high-temperature LCF and OP-TMF [4].

Though oxidation was considered as one of the main damage mechanisms of OP-TMF, Huter reported that the oxidation damage occurs only if, with enough electrolyte during TMF, this may have little influence on TMF endurance which is not a primary influence on TMF behavior [79].

2.5 TMF lifetime characterization and prediction

Due to the complex damage behavior, the TMF lifetime is difficult to predict. Many methods have been proposed or developed for TMF lifetime prediction. Manson made a study on thermal stress and pointed out the complexity of TMF in the early 1950s [97]. Later, Manson proposed the strain-range partitioning (SRP) method to evaluate TMF lifetime. Coffin modified the model based on the Manson-Coffin equation. Neu and Sehitoglu reviewed the damage mechanism of creep, fatigue, and oxidation, a model based on these damage mechanisms is used for TMF lifetime prediction of 1070 steel [4]. Sehitoglu also investigated the stress-strain behavior of cast 319 alloys with different secondary dendrite arm spacing (SDAS) and under

thermo-mechanical loading conditions by using a unified constitutive model [4, 5]. Miller model based on the accumulation of damage rates [98].

J-integral model is used to characterize the TMF behavior based on the fracture mechanics (crack initiation and crack growth behavior) [99]. Okazaki concluded that the rate of crack propagation is correlated with the range of cyclic J-integral, and followed a linear relationship on a log-log plot regardless of materials, test conditions, and crack configurations [100].

Takahashi estimate the thermo-mechanical deformation and fatigue life of the AC2B-T6 aluminum alloy by performing OP-TMF test with different ductile amplitude, ductile period, and temperature range, and introduced a new index of ‘plastic work density per second’ based on the conventional concept of plastic strain energy density to improve the accuracy in determining the fatigue life of the material [101].

Smith et al presented a modified two-state-variable unified creep-plasticity constitutive model for high-temperature stress-strain behavior of 319-T7 cast aluminum alloy. It can characterize the main deformation mechanisms and microstructural changes as a function of temperature and inelastic strain rate and also accurately simulate experimental stress-strain behaviors such as strain-rate sensitivity, cyclic softening, aging effects, and stress relaxation [102].

Minichimayr evaluated the Neu/Sehitoglu damage rate model for fatigue analysis of aluminum engine components. They reported that this model is suitable to describe the lifetime behavior at elevated temperatures and complex LCF and TMF loading, the model works fine in the temperature range from room temperature to 300°C for the cast aluminum alloy.

However, the greatest disadvantage of the Sehitoglu model is the number of necessary parameters, which mostly have physical meaning but are difficult to determine in the case of aluminum alloys. The Neu/Sehitoglu model is implemented in commercial fatigue analysis software and can fulfill the evaluation of life with little effort [73].

The hysteresis energy model is based on the dissipated energy of each TMF cycle [103, 104]. Among all these methods and models, the energy-based model is considered a better way for TMF behavior characterization and TMF lifetime prediction. As this method is based on the dissipated energy of each fatigue cycle, the energy-based model can involve process variables such as different temperature ranges, dwell time, strain, and stress amplitude [104, 105]. What's more, the energy-based model can characterize the TMF behavior with fewer parameters. Compared with other models or methods, usually, one or two parameters for the energy-based model are sufficient for calculations [106].

Minichmayr et al. discussed the Neu-Sehitoglu model on evaluation of TMF and LCF lifetime on aluminum alloy. Though the model gives the best accuracy on describing the complex LCF and TMF loading and their lifetime behavior at elevated temperature, a large number of parameters are necessary for the Neu-Sehitoglu model, which mostly has physical meaning but is difficult to determine in the case of aluminum alloys. They also investigated the energy-based approaches which use only one or two parameters while the damage mechanisms are together described, a non-conservative prediction occurs when the dominating damage mechanism changes or an additional mechanism appears [73].

Wang et al. investigated the LCF and TMF behavior of Al-Si piston alloy, they proposed a new energy-based model for LCF and TMF life prediction based on the hysteresis energy with strain rate modification [107]. They also proposed constraint factor, defined as the

ratio of the mechanical strain amplitude to thermal strain amplitude, which gives modification to the equations and provides acceptable accuracy on presenting TMF lifetime behavior [108].

2.6 Summary

Generally, a large number of researchers investigated the mechanical properties of Al-Si cast alloy, few of them focused on the TMF behavior. Besides, research on the effect of Mo strengthening effect on Al-Si cast alloy is limited. Therefore, investigation on elevated temperature properties of Al-Si cast alloys by TMF tests and the strengthening effect of Mo on Al-Si cast alloys is necessary.

CHAPTER 3 EXPERIMENTAL PROCEDURES

3.1 Materials

Four Al-Si cast alloys (319/319M, 356/356M) were prepared under laboratory conditions in the present work. Commercially pure aluminum (99.7%), together with pure Mg (99.9%), Al-50%Si, Al-25%Mn, Al-50%Cu, Al-10%Sr, and Al-TiB were used for master alloys. Master alloys were melted and stirred to homogenize in a clay-graphite crucible at 780°C in an electric resistance furnace with a protective atmosphere. After holding for 30 minutes to dissolve alloy elements and 15 minutes' degassing with high purity Argon gas, the alloys were cast into a pre-heated (400°C) permanent mold to obtain cylindrical test bars for TMF tests and microstructure investigation. Optical Emission Spectroscopy (OES) technique was used to examine the final compositions of the test alloys and presented in Table 3.1.

Table 3.1 Chemical composition (wt. %) of experimental alloys

Alloy	Si	Cu	Mg	Mn	Fe	Ti	Sr	Mo	Al
319	5.93	3.34	0.12	0.284	0.307	0.11	0.0106	-	Bal.
319M	6	3.5	0.1	0.3	0.3	0.1	0.01	0.3	Bal.
356	7.27	0.60	0.34	0.206	0.109	0.21	0.0113	-	Bal.
356M	6.99	0.61	0.38	0.219	0.111	0.23	0.0111	0.3	Bal.

3.2 Heat treatment

An electrically heated, air circulating chamber furnace was used for heat treatments. Both 319/319M and 356/356M alloys take 2-steps solution treatment, to prevent possible incipient melting of Cu-containing phases and present optimum condition of dispersoids [10]. All samples were quenched in water at room temperature after solution treatment. The aging process was held at 200°C for 5 hours to fulfill T7 over-aged temper. Detailed heat treatment parameters for tested alloys are summarized in Table 3.2.

Table 3.2. Heat treatment parameters for experimental alloys.

	1st step solution	2nd step solution	Aging
319	495°C/4h	515°C/2h	200°C/5h
319M			
356	500°C/4h	540°C/2h	
356M			

3.3 Thermo-mechanical fatigue test

The out-of-phase (OP) TMF was performed under strain control based on accepted code-of practice and ASTM E2368-10 standard [109, 110], where the mechanical strain is maximum at minimum temperature. All TMF tests were held under a temperature range between 60°C-300°C with a temperature changing rate $T=5^{\circ}\text{C/s}$, and 5s of dwell time at minimum/maximum temperature. The mechanical strain amplitude of 0.2%, 0.4%, and 0.6% was applied to all tested alloys.

Cylindrical TMF specimens, with a parallel gauge section of 75mm long and 10mm in diameter with a 5mm diameter air hole, were machined from T7-treated samples in accordance with ASTM: E606 standard [111-113]. Detailed dimensions and geometry of TMF specimens are shown in Figure 3.1.

TMF tests were held by Gleeble 3800 thermal-mechanical simulator system. Samples were heated by Joule's heating system and cooling was achieved by compressed air through the hollow tube specimen. The thermal gradient in the gauging zone was controlled within 5% of the target temperature. Before each TMF test, a series of pre-cycling procedures were finished, including sample installation, Young's modulus measurement, multi-cycle thermal strain measurement, and the zero stress adjustment.

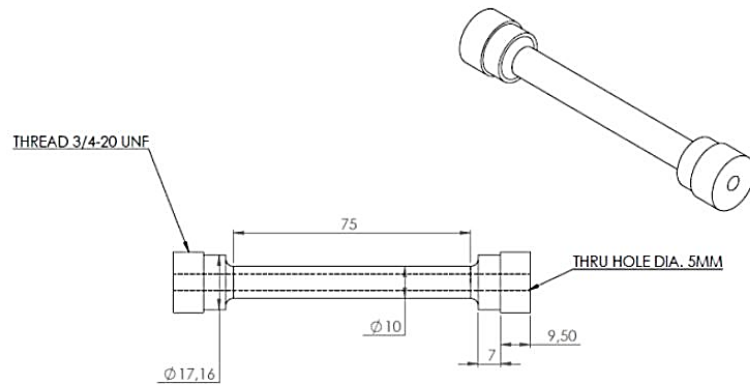


Figure 3.1 Geometry and dimension of thermo-mechanical fatigue test sample (unit in mm) ©The Minerals, Metals & Materials Society 2019 [113].

TMF test is terminated when a predefined criterion is reached, for example, a pre-set number of cycles or a drop of 60% in initial min/max stress. The fatigue life was considered as the number of cycles when the TMF test terminated. Once the tests were finished, samples were pulled to fracture for crack behavior characterization.

3.4 Microstructure characterization

3.4.1 Sample preparation

All metallographic samples for microstructural characterization were cut from raiser bars and after fatigue samples. Samples were mounted by conductive graphite powder filler. The mounted samples were ground with a series of SiC grinding papers (#120, #240, #320, #600) with water lubricant in each grinding step. Polishing was followed with 6 μ m and 1 μ m diamond polishing paste and diamond extender as a lubricant. Final polishing was carried out with colloidal silica suspension and performed on a silk polishing pad.

3.4.2 Optical microscopy

A computerized Nikon Eclipse ME600 optical microscopy (OM) with CLEMEX VISION PE software was used for microstructure investigation and analysis, including the intermetallic phases and their evolution after various TMF tests as well as the fracture surface analysis.

3.4.3 Scanning electron microscopy

JEOL JSM-6480LV scanning electron microscopy (SEM) equipped with energy-dispersive X-ray spectroscopy (EDS) was used to identify intermetallic phases, fracture analysis and obtain high magnification images.

3.4.4 Transmission electron microscopy

JEOL JEM-2100 transmission electron microscopy (TEM) equipped with energy-dispersive X-ray spectroscopy (EDS) was used for precipitates identification and analysis.

Samples for TEM observation were cut from the gauge zone of the TMF test samples and punched into 3mm diameter disk. Samples were ground by #600 SiC grinding papers with water lubricant followed with colloidal silica suspension on silk polishing pad to reduce the sample thickness to 40-60 μ m. After that the twin-jet electrical polish method with the solution of 75mL Nitric acid in 250mL methanol at -30 $^{\circ}$ C was used to create TEM observation region on samples.

CHAPTER 4 THERMO-MECHANICAL FATIGUE PROPERTIES OF AL-SI 319 AND 356 CAST ALLOY

The Al-Si alloys that are usually used for engine components fabrication can be classified into two main categories. One stands for Al-Si-Cu alloy such as 319 alloys, which exhibits higher yield and creep strength above 200°C but present lower ductility, the other one stands for Al-Si-Mg alloy such as 356 alloys, which presents high ductility and acceptable strength at ambient temperature but the strength decreases significantly above 200°C [3].

In this chapter, a detailed description of TMF test results of 319 and 356 alloy under T7 heat treatment was given, followed by a discussion of the relationship between the TMF behaviors and microstructure of alloys.

4.1 TMF behaviors

4.1.1 Cyclic stress-strain behavior

Figure 4.1 shows the stress-strain hysteresis loops of the initial cycles, mid-life cycle, and end-life cycle at a mechanical strain amplitude of 0.2%, 0.4%, and 0.6% for 319 and 356 alloys under a temperature range of 60°C to 300°C.

In general, it can be observed asymmetrical hysteresis loops in all tested strain amplitudes in 319 and 356 alloys, which are considered affected by a variety of thermally activated processes due to the specimen crossing a temperature range during TMF. The tensile stress level is higher than the compression stress level, presenting tensile mean stress, which is the typical feature of hysteresis loops for OP-TMF loading. From 0.2% to 0.6%, as the strain

amplitude increased, the shape of the hysteresis loop is wider in the initial cycles, which indicates a larger proportion of plastic strain in mechanical strain. With the fatigue life increasing, the shape of the hysteresis loop in the mid-life cycle and end-life cycle become flattered in all strain amplitude. On one hand, the width of strain range at zero stress increase with TMF cycles, which represents increasing the plastic strain. On the other hand, the maximum and minimum stress decrease with TMF cycles, which refers to cyclic softening behavior, attribute to the plastic deform accumulation in each TMF cycle, further the plastic deformation leads to crack propagation and load capacity reduction.

For both 319 and 356 alloy, the minimum stress from initial TMF cycles is around 100MPa in all strain amplitudes and gradually decreases with TMF cycles due to cyclic softening. However, though maximum stress also decreases with TMF cycles, 319 alloy shows higher maximum stress levels than 356 alloys from initial cycles. Besides, the width of strain range at zero stress in 356 alloys is wider than 319 alloys at initial cycles in all strain amplitudes, which indicates higher plasticity of 356 alloys.

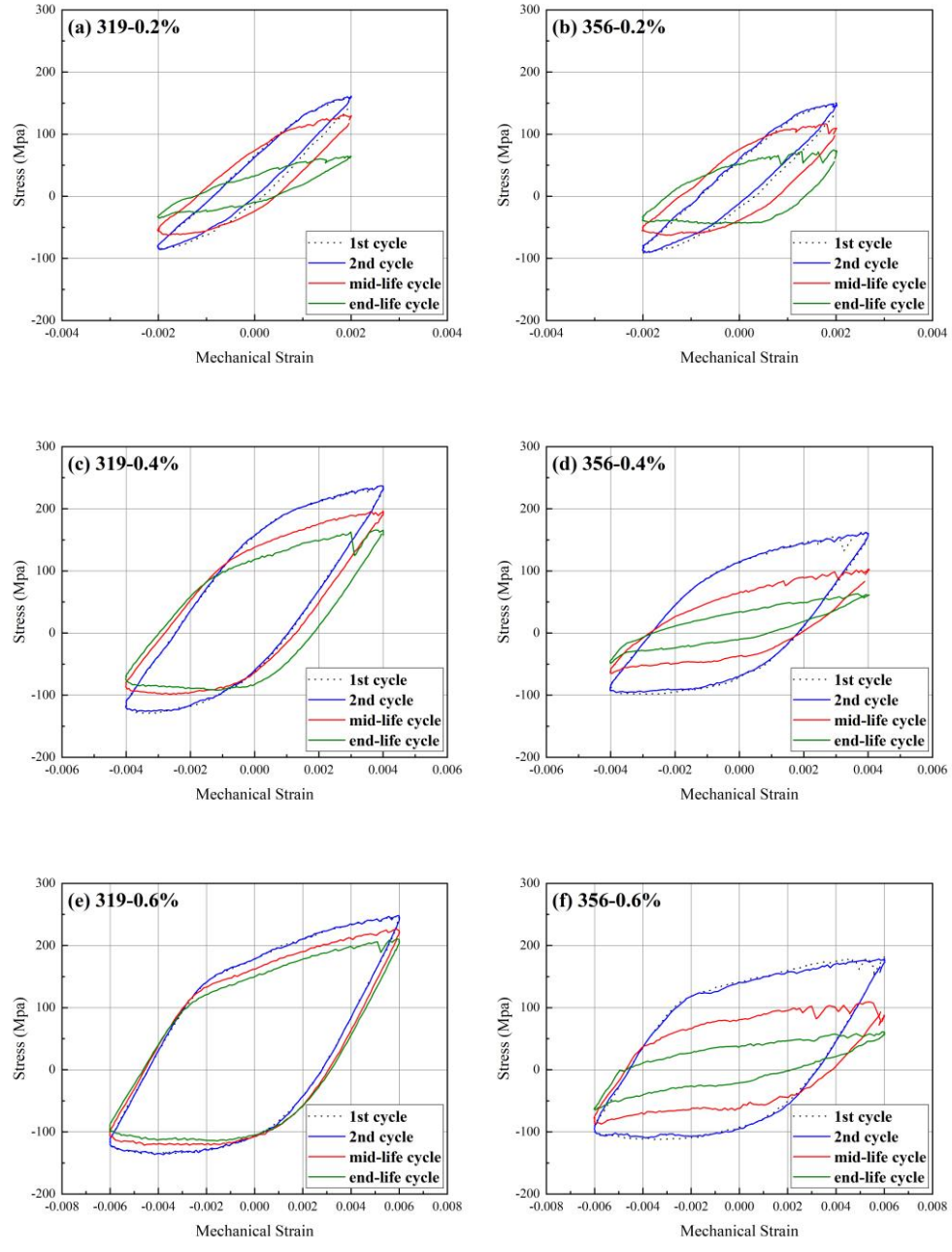


Figure 4.1 Stress-strain hysteresis loops under OP-TMF loading conditions of 319 and 356 alloy.

(a) 319-0.2%, (b) 356-0.2%, (c) 319-0.4%, (d) 356-0.4%, (e) 319-0.6%, and (f) 356-0.6%

© Shuai Wang, 2021

During TMF, cyclic evolution of plastic strain is important to evaluate the mechanical behavior of specimens. According to the definition, the total strain (ϵ_{total}) is the sum of elastic

strain (ε_{el}) and plastic strain (ε_{pl}). In this study, the width of the strain range at zero stress in the hysteresis loop is used as the value of the plastic strain amplitude. The plastic strain evolution with fatigue cycles at different strain amplitudes of 319 and 356 alloys is plotted in Figure 4.2. In all TMF tests, the specimen experienced a slight decrease in plastic strain for the initial few cycles, then followed with a continual increase with fatigue processing, which indicates cyclic hardening and cyclic softening behavior, respectively. As seen in Figure 4.2, the initial plastic strain increases with increasing the mechanical strain. 356 alloy shows higher plastic strain than 319 alloys among all strain amplitudes, which indicates higher ductility of 356 alloys. It can be noticed that 356 alloys at 0.4% and 0.6% strain amplitude occur a significant decrement several cycles before failure, while for 319 alloys, the plastic strain still presents an increasing tendency at ending cycles. This phenomenon can be related to the final failure of 319 and 356 alloy. Most test specimens of 319 alloys fractured into two pieces when the TMF test end while specimen of 356 alloys only show large crack within, which can indicate that 319 alloy reaches fracture failure during plastic accumulation and happens quickly, while for 356 alloys, crack growth is relatively slow, the plastic strain decrement in ending cycles can be referred as material endurance decrement as the crack growth to a critical size.

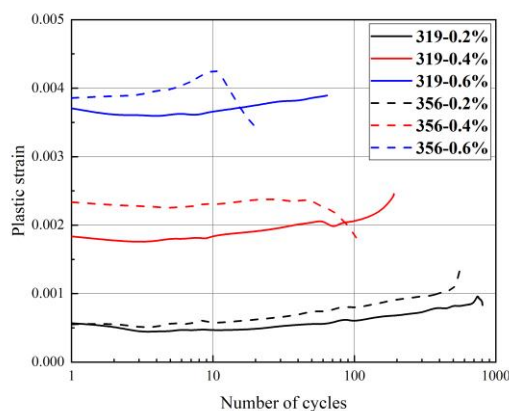


Figure 4.2 The plastic strain of 319 and 356 alloy under OP-TMF loading at different strain amplitude.

Figure 4.3 shows the cyclic stress evolution with fatigue cycles at different strain amplitude for 319 and 356 alloys, respectively. Among all strain amplitudes, the initial tensile stress value is higher than the initial compression stress value, which contributes to the higher yield strength at a lower temperature. As the strain amplitude increases, the peak stress amplitude increases, and the fatigue lifetime decrease for both 319 and 356 alloys. The cyclic softening behavior can be observed from the graph as both tensile and compression stress gradually decreases with the fatigue cycle in all strain amplitude.

According to Huter, the stress level can be interpreted as a superposition of hardening, softening, and large crack growth at the end of fatigue life [80]. It can be noticed in Figure 4.3 that there is an inflection point (indicated by the arrow, where there is a sharp change on the stress change with cycle) in the curve for both 319 and 356 alloys, at which TMF can be divided into two different stages. Stage I begins at the initial fatigue cycle until it reaches the inflection point. In this stage, stress level gradually decreases due to cyclic softening behavior and microstructure damage. The followed Stage II starts from the number of cycles where the inflection point occurs until the specimen reaches final failure. In this stage, the rapid decrease in stress can be attributed to the large crack formation by exceeding a critical crack length. It can be observed that 356 alloy has an early occur inflection point than 319 alloys under each tested strain amplitude, which resulted in early fatigue damage of 356 alloys. After this point, the stress drops more rapidly for 319 alloy than 356 alloy, due to the fast growth of microscopic and macroscopic cracks. Though 356 alloy shows a lower crack growth rate in stage II, the earlier initiation of microcracks limited the fatigue life of 356 alloys.

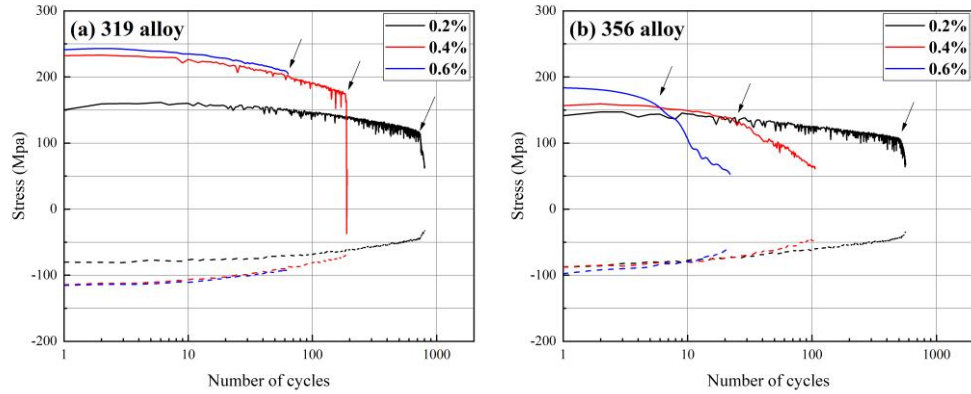


Figure 4.3 The evolution of maximum and minimum stress at different strain amplitude for (a)319 alloy and (b) 356 alloy. © Shuai Wang, 2021.

For a better comparison, the proportion of stage I in the total lifetime of 319 and 356 alloys have been calculated and listed in Table 4.1. In 319 alloy, stage I takes over 90% of a total lifetime among all tested strain amplitude, the 100% in 319-0.6% represents there is no macro damage before the end TMF test. While for 356 alloys, the stage I proportion in total lifetime is 85% at 0.2% strain amplitude, slightly lower than 319 alloys under the same condition. For 356 alloys under 0.4% and 0.6% strain amplitude, stage I only take 22% and 27% in total TMF lifetime, which is significantly lower than 319 alloys under 0.4% and 0.6% strain amplitude.

Table 4.1 Proportion of stage I in total TMF lifetime of 319 and 356 alloy at different strain amplitudes

Strain\Alloy	319 alloy	356 alloy
0.2%	90%	85%
0.4%	96%	22%
0.6%	100%	27%

4.1.2 Lifetime behavior

Figure 4.4 summarizes the TMF lifetimes of 319 and 356 alloys under different strain amplitudes of OP-TMF loading conditions. In general, the fatigue life decreases with increasing strain amplitude and is approximately under linear relations when plotted on a log-log scale for both 319 and 356 alloys. At lower strain amplitude, like 0.2%, both 319 and 356 alloys show similar average TMF life, while the results of 319 alloys show higher dispersion degree. Though 319 and 356 alloys show similar maximum TMF lifetime at 0.4% strain, 319 alloys show 2 times longer average TMF lifetime than 356 alloys at 0.4% strain amplitude and 4 times longer TMF lifetime than 356 alloys at 0.6% strain.

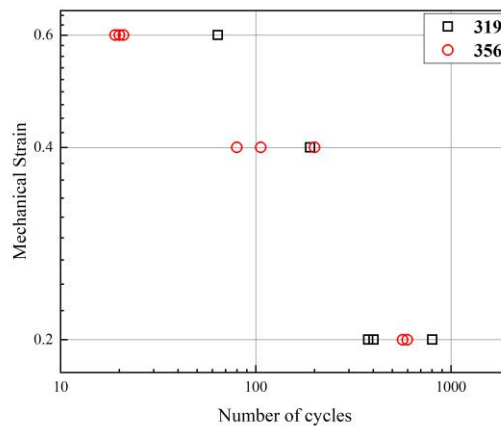


Figure 4.4 Mechanical strain amplitude vs number of cycles for 319 and 356 alloy under OP-TMF loading. © Shuai Wang, 2021

4.1.3 Microstructural observation

4.1.3.1 Initial microstructure

The microstructure of 319 and 356 alloys was investigated before and after TMF tests. Low-magnification images were obtained by optical microscope. Figure 4.5 shows the typical

microstructure of 319 and 356 alloy, respectively. As can be seen, both 319 and 356 alloys consist of the primary α -Al dendrites and connected eutectic Si particles as well as intermetallic phases located in the interdendritic regions. Eutectic Si particles (dark grey particles in Figure 4.5) in both 319 and 356 alloys are similar in size and morphology, which can attribute to the modification effect of Sr. Intermetallic phases were identified by EDS analysis, which is observed as α -Al-(Fe, Mn)-Si phase with a Chinese script morphology (grey particles in Figure 4.5), no other Fe-bearing phases observed in 319 and 356 alloys.

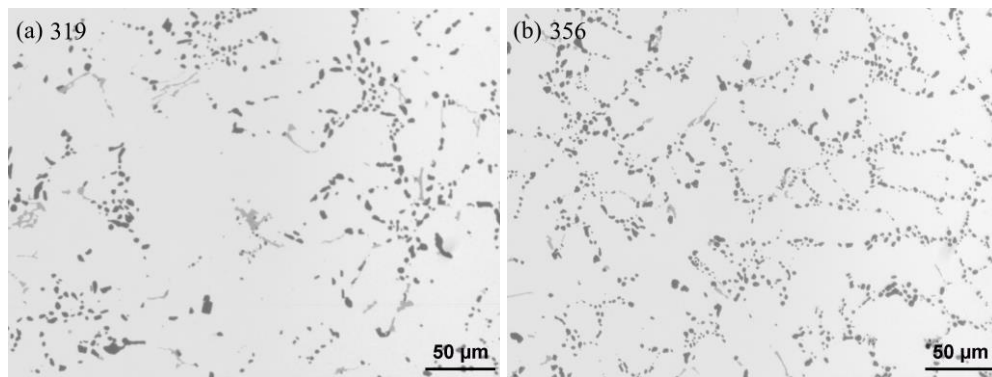


Figure 4.5 Microstructure before TMF of (a) 319 alloy and (b) 356 alloy. © Shuai Wang, 2021

By using the analysis software, a few intermetallic phases properties are investigated and listed in Table 4.2. As seen below, the average size of eutectic Si particles in 319 alloys is slightly larger than 356 alloy, with lamellar morphology of eutectic Si phase and large volume fraction of other intermetallics, 319 alloy is more likely to have microstructure damage than 356 alloys during TMF.

Table 4.2 Analysis results of microstructure of 319 and 356 alloy before TMF

	319 alloy	356 alloy
Morphology of eutectic Si	Lamellar/globular	Globular/granular
Sphere.Diam. of eutectic Si	4.0 μ m	3.5 μ m
Area fraction of other IMCs	1.6%	0.8%

4.1.3.2 Evolution of precipitation during TMF

As typical precipitation strengthening alloy, the precipitates in both 319 and 356 alloys play an important role in alloys' mechanical properties. The TMF behavior can be represented by the change of precipitates during TMF. Nanosize precipitates in both 319 and 356 alloys were investigated before and after various strain amplitudes of TMF tests by TEM. The precipitation observation result for 319 and 356 alloys before the OP-TMF test are shown in Figure 4.6. Both 319 and 356 alloys can be observed a large amount of nano-sized precipitation in the Al matrix. The precipitates were identified as plate-like θ' -Al₂Cu phase in 319 alloy and needle-like β' -Mg₂Si phase in 356 alloys, respectively. Besides, both 319 and 356 alloys can observe α -Al-(Fe, Mn)-Si dispersoids in the Al matrix, as EDS results shown in Figure 4.7.

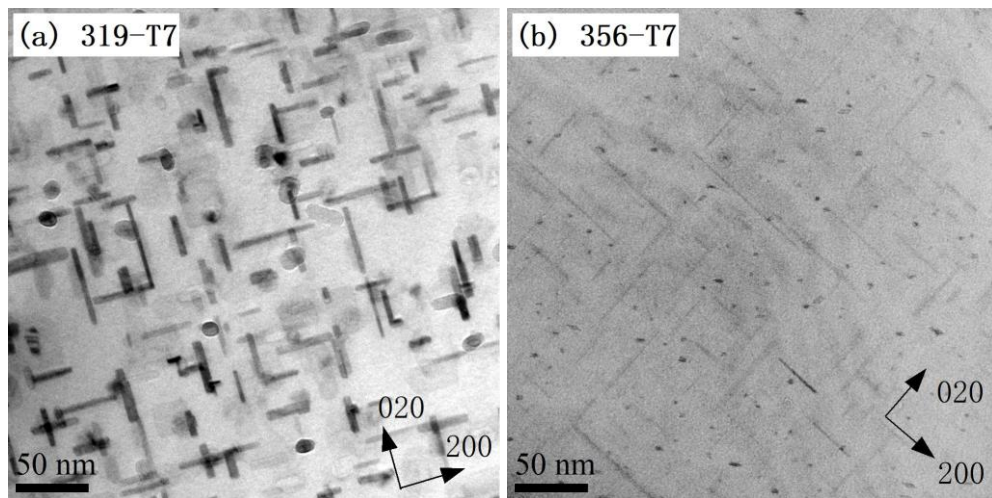


Figure 4.6 The TEM microstructure before TMF of (a) 319-T7 and (b) 356-T7. © Shuai Wang, 2021

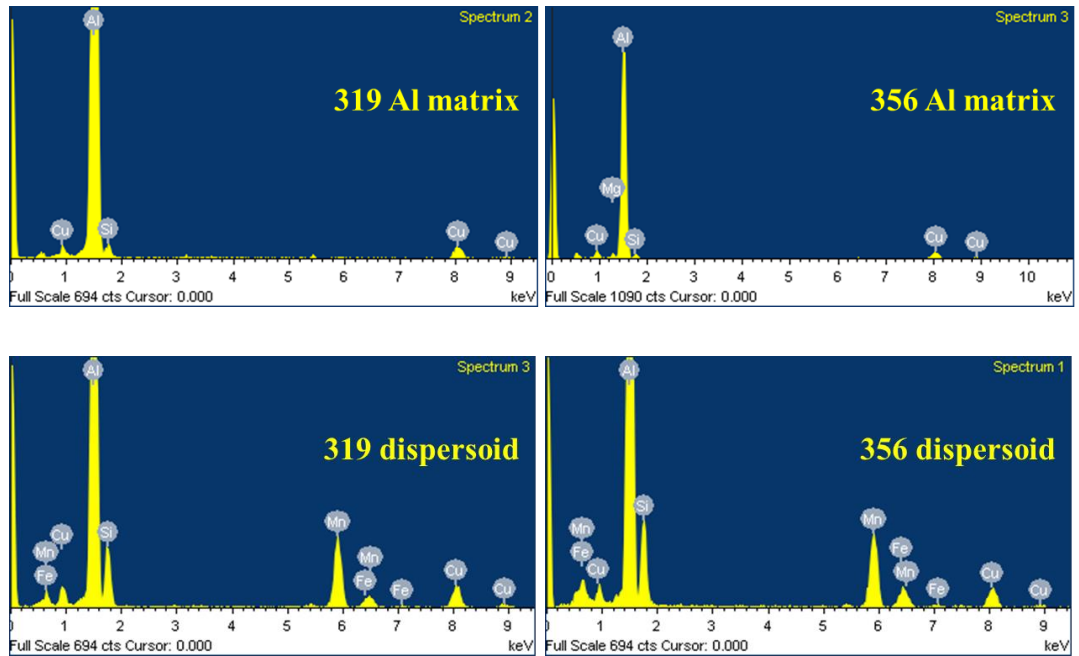


Figure 4.7 EDS spectrums confirm the composition of Al matrix and dispersoids of 319 and 356 alloys. © Shuai Wang, 2021

Figure 4.8 presents the precipitate observation results after different strain amplitudes of TMF tests for 319 alloys. Compared with the microstructure before TMF, the number of plate-like θ' - Al_2Cu phases after TMF tests were decreased. θ' - Al_2Cu phase is observed to grow after TMF in all tested strain amplitude. For 0.6% strain amplitude, the growth is more obvious in the width direction than the length direction.

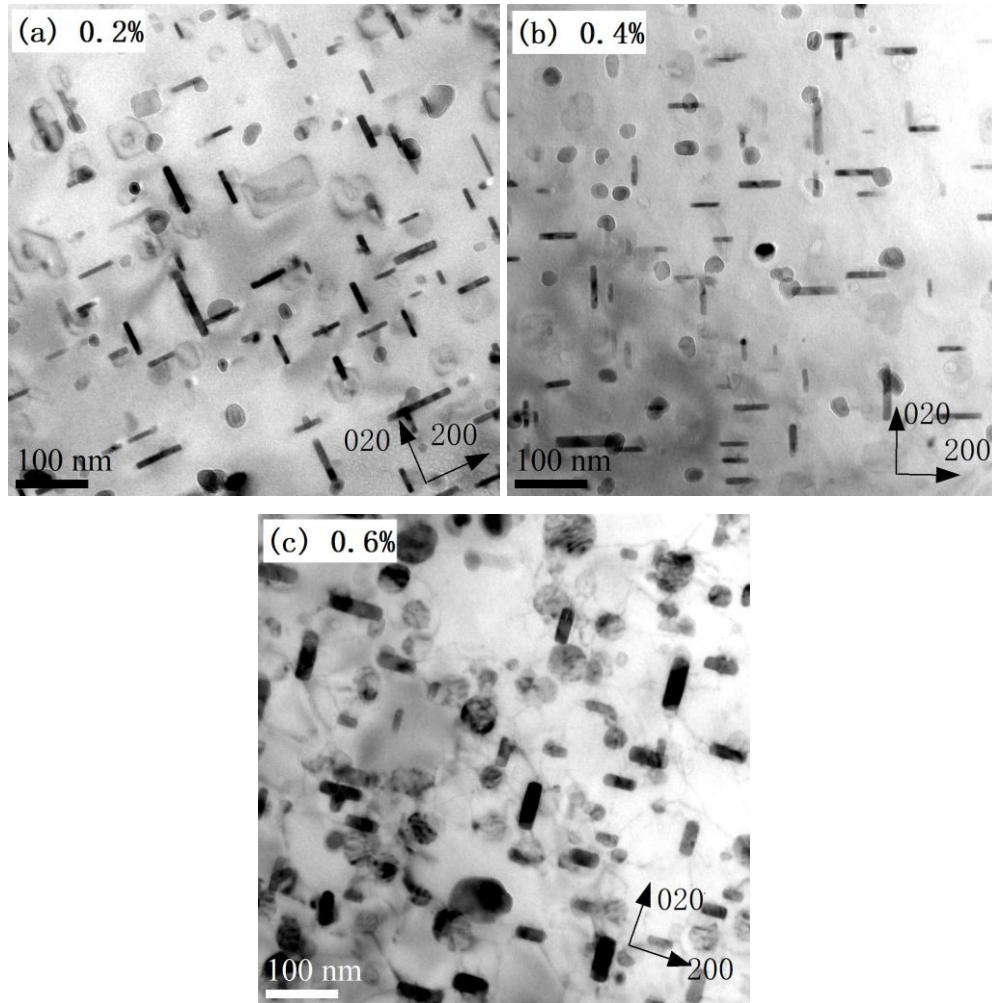


Figure 4.8 Precipitates microstructure of 319 alloy after TMF, the loading direction is perpendicular to the image, (a) 0.2%, (b) 0.4% and (c) 0.6%. © Shuai Wang, 2021

Figure 4.9 shows the precipitates of 356 alloy after different strain amplitudes of the TMF test. Compared with Figure 4.6(b), the needle-like β' - Mg_2Si phase is coarsened to the rod-like β' - Mg_2Si phase after TMF. The number of precipitates decreases significantly after TMF tests. Besides of β' - Mg_2Si phase coarsening, the Q- $\text{Al}_5\text{Mg}_8\text{Cu}_2\text{Si}_6$ phase is formed after TMF, which does not occur before TMF.

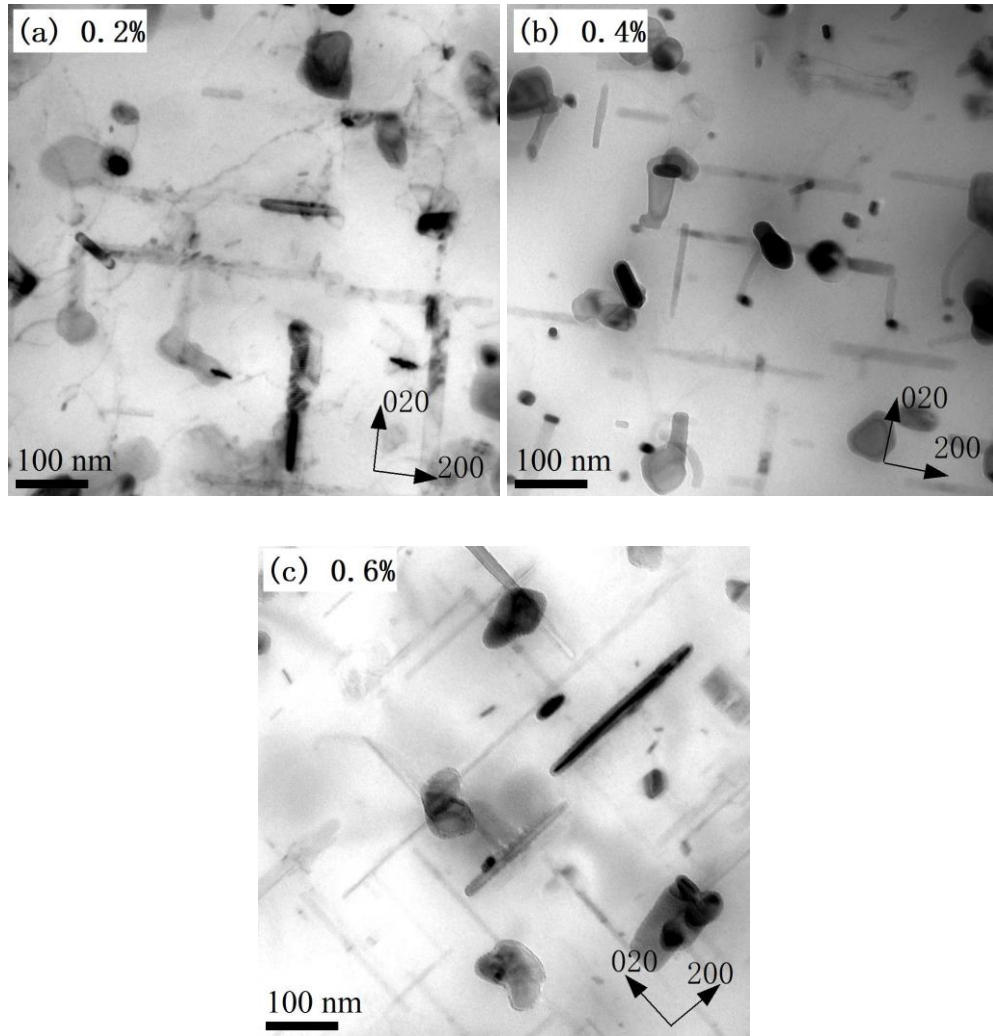


Figure 4.9 Precipitates microstructure of 356 alloy after TMF, the loading direction is perpendicular to the image, (a) 0.2%, (b) 0.4% and (c) 0.6%. © Shuai Wang, 2021

After the quantification, the precipitates parameters such as length, thickness, and number density before and after the TMF test of 319 and 356 alloys are listed in Table 4.3. Both 319 and 356 alloy contains a large number of nano-sized precipitates before TMF. Coarsening behavior of precipitates can be seen in both length and width direction after TMF. The number density of precipitates decreases significantly in 319 and 356 alloy, and the degree

of decrement is lower at high strain amplitude, which is related to the different exposure times under various strain amplitude.

Table 4.3 Parameters of precipitates of 319 and 356 alloys

Alloy	Status	Precipitates length (nm)	Precipitates width (nm)	Number density (μm^{-1})
319	Before TMF	24.05	2.14	4451.2
	After 0.2%	57.94	6.04	501.4
	After 0.4%	41.97	4.99	789.8
	After 0.6%	40.07	9.03	690.6
356	Before TMF	35.01	1.38	19144.8
	After 0.2%	165.54	7.46	191.1
	After 0.4%	102.38	7.29	253.7
	After 0.6%	102.4	6.28	394.0

Coarsening of precipitates during fatigue will change the mechanical properties of the alloys, thus the coarsening rate of precipitates can be used for evaluating the TMF behavior. The Lifshitz-Slyozov-Wagner (LSW) model was proposed to calculate the coarsening rate of precipitates. The LSW equation can be expressed as Equation 2 below [114]:

$$L^n - L_0^n = k \cdot t \quad \text{Equation 2}$$

where L is the average half-length of precipitates after TMF, L_0 is the average half-length of precipitates before TMF, k is the coarsening rate constant, t is the time of TMF process, and n is the temporal exponent. The value of n depends on the coarsening mechanisms controlled by volume diffusion ($n=3$) [115-117] and interface kinetic ($n=2$) [118, 119]. Some researchers have suggested that the growth of the plate-like θ' -Al₂Cu precipitates is prone to obey the $t^{1/2}$ law ($n=2$), as the interface reaction dominant coarsening [120-122].

Besides, the value of t normally uses the second total time passed as the unit for softening rate calculation, while in TMF, the temperature changes in each fatigue cycle, which means the coarsening rate per second may not even due to the temperature difference in each cycle. Therefore, in our case, the value of t is using the number of TMF cycles.

By using the length parameters listed in Table 4.3, the coarsening rate of 319 and 356 alloys are calculated and plotted in Table 4.4. In general, for both $t^{1/2}$ law and $t^{1/3}$ law, the k value increases with strain amplitude increasing, which means higher strain amplitudes result in a higher coarsening rate of precipitates. In a comparison of both alloys, 356 alloy shows a much higher coarsening rate than 319 alloys in each strain amplitude

Table 4.4 Coarsening rate constant k after various strain amplitude OP-TMF

k value	$t^{1/2}$ law results		$t^{1/3}$ law results	
	319 alloy	356 alloy	319 alloy	356 alloy
After 0.2%	3.45	43.85	224.62	7527.72
After 0.4%	6.22	87.32	381.21	9719.85
After 0.6%	16.05	463.01	788.03	51546.52

During low temperature, dislocations are produced in the Al matrix under cyclic loading and substructures like dislocation cells and walls can be formed. When the temperature increases, the annihilation of dislocation or reconstruction of dislocation substructure occurs, which results in a decrease of slide resistance and improved the soften effect and plastic deformation of the matrix. Meanwhile, due to the Orowan effect and dynamic recovery, the interaction between dislocation and precipitates decreases during cyclic loading. Besides, the different morphology of plate-like θ -Al₂Cu precipitates in 319 alloy and needle-like β -Mg₂Si precipitates in 356 alloys is also a factor of different coarsening rates during TMF. As the

existence of a large negative misfit in the perpendicular direction is relative in the plate surface, θ -Al₂Cu phases have preferential orientation mechanisms during OP-TMF [93, 94].

In conclusion, precipitates from 319 and 356 alloys gradually coarsened and lost coherency with matrix, and precipitates number density reduced due to Ostwald ripening [123-125], the effect for precipitates preventing dislocation movement is decreased as precipitates coarsened during TMF, resulting in a reduction of strengthening effect and it is the main reason for cyclic softening behavior during fatigue. Higher precipitates coarsening rate and higher decrement on the number density of precipitates in 356 alloys promote plastic deformation during TMF, present as the higher softening rate on stress level than 319 alloys.

4.1.3.3 Fractography

The crack behavior is reviewed and discussed by many researchers [79, 80, 107, 108, 123]. The damage behavior under TMF loading depends on cyclic temperature and accumulation of plastic stress/strain. In Al-Si alloys, precipitation strengthening and dispersoid strengthening are two main methods that provide the strength of the alloy. In which the weakening of strengthening effect at high temperature such as cyclic aging, coarsening, and dissolution of precipitates is important for alloy failure.

As previously discussed, precipitates coarsening will happen under elevated temperature exposure, leading to reduced strengthening effect on α -Al matrix, behave as softening behavior, and reduced hardness for α -Al matrix. While other phases such as eutectic Si particles and α -Al₁₅(Fe, Mn)₃Si₂ phases shows good stability and have minor changes in mechanical properties at elevated temperature. Thus, the continuous thermal/mechanical cyclic loading during TMF leads to a greater mismatch between ductile α -Al matrix and hard phases,

resulting in localized plastic deformation and microcracks initiation. Besides the mismatch between matrix and hard phases, the phase angle between mechanical and thermal loading is another important factor that affects the fatigue damage mechanism.

For OP-TMF loading, the tensile strain occurs at low temperature and compressive strain at high temperature. At low temperatures, the plastic deformation is dominated by dislocation slip [123]. The nano-size precipitations prevent dislocation movement. The tensile stress act on the eutectic Si phase and Fe-bearing intermetallics are high at low temperature. At high temperatures, the deformation is driven by the plastic flow of the α -Al matrix [126]. Stress relaxation can be found under elevated temperature process and damage on hard phases are relatively small under high-temperature compression stress. This indicates that tensile stress is the key factor to OP-TMF damage behavior, as hard phases fracture during the low-temperature region of OP-TMF and promote crack initiation and growth during cyclic deformation.

The fracture behavior of 319 and 356 alloys after TMF tests was investigated by OM and SEM. Samples after TMF tests were cut and polished along the loading axis for crack observation. Figure 4.10 shows the OM observation results near fracture after TMF test for 319 and 356 alloys. As seen below, numbers of broken eutectic Si particles and Fe-bearing intermetallic phases can be observed in both 319 and 356 alloys after the TMF test, also few particles are observed debonded from the Al matrix. It can be assumed that cracks are more possible to propagate through those cracked and/or debonded particles. For 319 alloy, which contains a larger eutectic Si phase and higher volume fraction of Fe-bearing intermetallics, have higher tendency to occur microstructure damage on these phases during TMF, and crack growth can be easier by the coalescence through these fractured particles. While for 356 alloy, the matrix strength decreases quicker than 319 alloy due to the higher coarsening rate of β -

Mg₂Si precipitates in 356 alloy, the inhomogeneous plastic deformation forms persistent slip bands and helps open transgranular cracks during TMF tests.

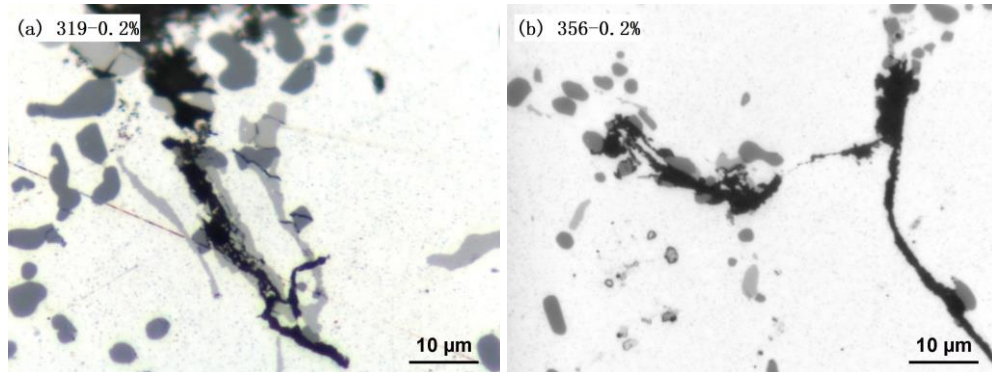


Figure 4.10 Crack microstructure after 0.2% TMF test of (a) 319 alloy and (b) 356 alloy. The loading axis is vertical. © Shuai Wang, 2021

The overall low magnification view for fracture surface of 319 and 356 alloys is observed by SEM, as shown in Figure 4.11. Porosity can be observed from both fracture surfaces, as marked in the pictures. In 319 alloys, porosity is relatively small and evenly spread in the sample. Crack ridges can be found on the fracture surface of 319 alloys, indicating that cracks may have multiple initiate sites and merge during fatigue failure. For 356 alloys, a large, continuous porosity can be found at fracture surface, crack initiated from porosity and an area around porosity can be seen as a crack growth area. The rest of part fracture surface of 356 alloy, which is take place after the TMF test is finished, the sample is pulled to fracture by for observation.

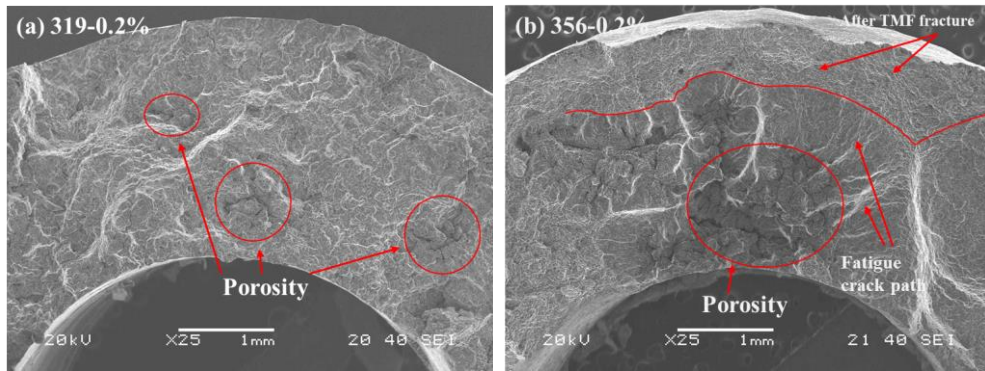


Figure 4.11 Overall view of fracture surface after 0.2% TMF test (a) 319 alloy and (b) 356 alloy.

© Shuai Wang, 2021

Figure 4.12 shows fracture morphology at the crack propagation area of 319 and 356 alloys. From the BSE photo of 319 alloys, a large number of bright phases are found from the crack path, identified as $\alpha\text{-Al}_{15}(\text{Fe}, \text{Mn})_3\text{Si}_2$ phases, and fractured eutectic Si particles can also be observed with. For 356 alloy, crack path through the $\alpha\text{-Al}$ matrix, limited numbers of eutectic Si and intermetallic particles can be found on the crack path, crack propagate transgranular and fatigue striation can be found along the crack growth direction.

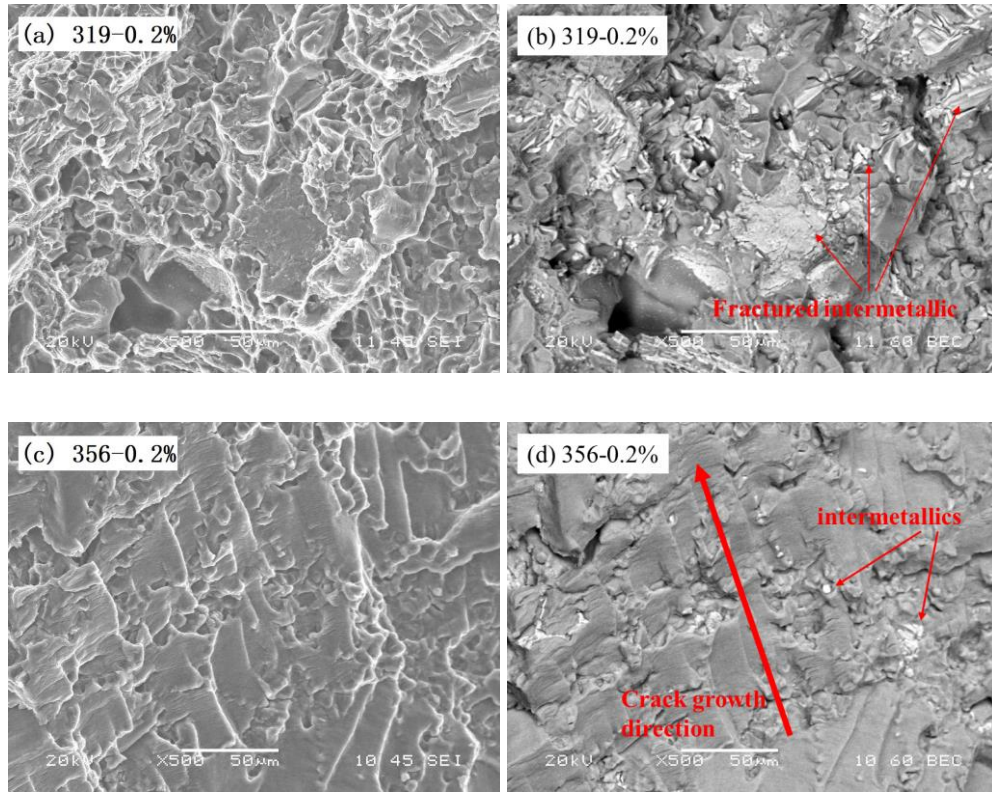


Figure 4.12 Fractography and BSE micrograph of fractured specimen after 0.2% TMF test. (a, b) 319 alloy and (c, d) 356 alloy. © Shuai Wang, 2021

To be concluded, the damage behavior of 319 and 356 alloys have some differences. In 319 alloy, which contain more intermetallic particles and larger eutectic Si, those hard phases break under tensile stress at low temperature, microcracks act as crack initiation spots, crack grow by coalescence of these fractured particles and finally reach fatigue failure. However, for 356 alloy, crack initiate from porosity and grow transgranular due to inhomogeneous plastic deformation, most crack path through the α -Al matrix than broken hard phases. Though 356 alloys show higher ductility, which may delay crack propagation, the high-stress concentration provided by porosity leads to earlier crack initiation and damage in 356 alloys, resulting in limited TMF lifetime.

4.2 TMF lifetime parameters

Fatigue damage and TMF lifetime behavior can be expressed by various models [4, 5, 73, 97-102]. According to previous research, the energy model was widely used for fatigue lifetime characterization and prediction. Different with cyclic strain method normally used in LCF, which is expressed in terms of elastic and plastic components of the total strain amplitude under stable temperature, known as Basquin and Coffin-Manson relation, respectively [127, 128]. These methods may not fit the TMF loading condition that the samples cross a temperature range, leading to a thermal strain during TMF processes. The hysteresis energy which involves both strain and stress amplitudes shows more rationality than stress or strain solely and can be used more reasonably to evaluate the fatigue property [107]. Figure 4.13 shows the schematic diagram of the hysteresis energy calculation [107].

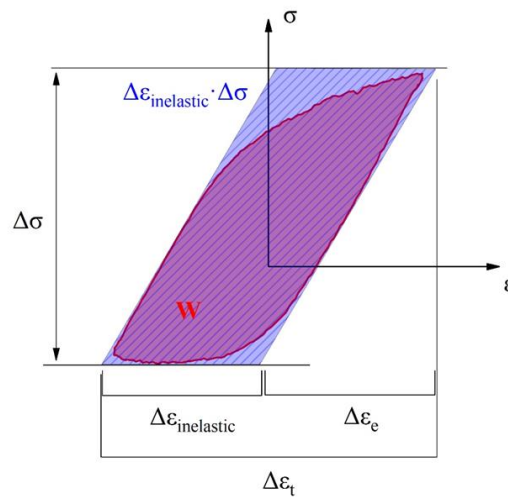


Figure 4.13 Schematic diagram of hysteresis energy model calculation © 2017 Elsevier B.V. [107].

The relation between plastic work energy W_i and the value of $\Delta\varepsilon_p \cdot \Delta\sigma$ can be expressed by Equation 3:

$$W_i = \int \sigma d\varepsilon = C \cdot \Delta\varepsilon_p \cdot \Delta\sigma \quad \text{Equation 3}$$

Here C is a constant named as the ‘shape factor’, which stands for the proportion of the i th hysteresis loop area W_i over the parallelogram area $\Delta\varepsilon_p \cdot \Delta\sigma$, which is related to external loading condition and cyclic stress-strain response of the material. The hysteresis energy involving both strain and stress amplitudes shows more reasonably to evaluate the fatigue properties than using stress or strain individually. The hysteresis energy is cyclic stable after adaption for several cycles for most applied strain amplitude of both alloys, as shown in Figure 4.14. As presented, the hysteresis energy exhibits cyclic stability after a short period of adaption for most applied strain amplitudes. For 356 alloy under 0.6% strain amplitude loading condition, an early energy loss can be found after the initial few cycles, which can be related to the early crack formation during TMF tests.

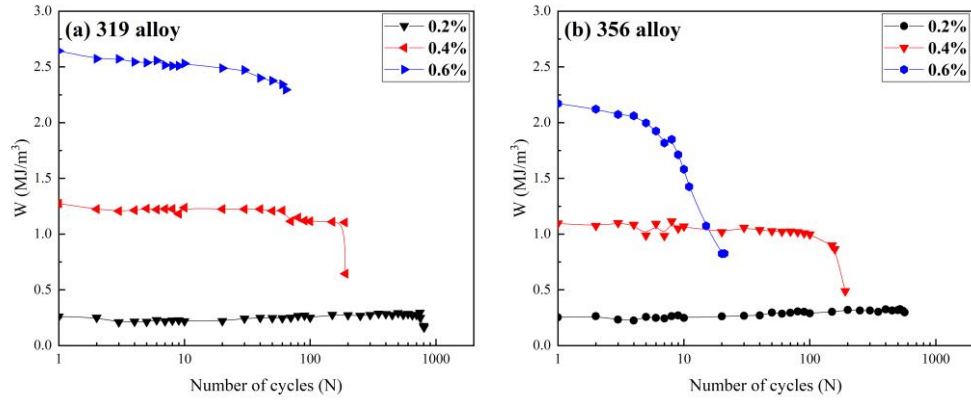


Figure 4.14 Hysteresis energy as a function of number of cycles for (a) 319 alloy and (b) 356 alloy.

© Shuai Wang, 2021

The equation of energy model for fatigue behavior characterization is listed as Equation 4 as below:

$$W_s = W_0 \cdot N_f^{-1/\beta} \quad \text{Equation 4}$$

where W_0 and β are material parameters. The W_0 indicates a fatigue damage capacity, the β represents the fatigue damage exponent, reflected in the slope of the $\log W_s - \log N_f$ relationship [107, 108]. The W_s is the saturation hysteresis energy obtained from the fatigue data at half lifetime ($N = N_f / 2$).

Based on the calculated data, the value of fatigue parameters for 319 and 356 alloys are listed in Table 4.5 and the TMF behavior expressed by equations are plotted in Figure 4.15. As seen below, the calculated energy parameters can characterize the fatigue behavior of 319 and 356 alloys. 319 alloys show a higher fatigue damage capacity value than 356 alloys, which represents the higher material yield strength of 319 alloys. The exponent value represents the

relation between TMF lifetime and hysteresis energy. The high value of the exponent is 356 alloys means TMF lifetime decrease significantly with hysteresis energy increasing. All tested TMF results fall within the 2 times scatter band based on the energy model. To be concluded, the hysteresis energy model can characterize the fatigue properties after TMF tests with several parameters.

Table 4.5 Value of parameters calculated by the hysteresis energy model

	W_0	β	C
319 alloy	167.43	0.98	0.91
356 alloy	5.06	2.39	0.84

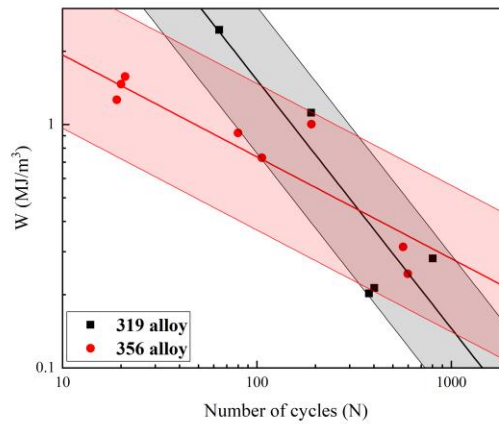


Figure 4.15 TMF lifetime results and Hysteresis energy model fitting results for 319 and 356 alloys.

© Shuai Wang, 2021

4.3 Summary

In this chapter, the TMF properties of 319 and 356 alloy, including cyclic stress-strain behavior, lifetime behavior, microstructure, and energy model parameters are investigated, the following conclusion can be drawn as below:

1. Both 319 and 356 alloys show cyclic softening behavior during TMF at all tested strain amplitudes, and asymmetrical hysteresis loops with tensile mean stress also can be found in both 319 and 356 alloys.
2. 319 alloy shows similar TMF life with 356 alloys at 0.2% and 0.4%, but longer TMF life at 0.6% strain amplitude.
3. After TMF, the number density of precipitates in both 319 and 356 alloys shows a significant decrease, indicating their coarsening during TMF. However, the coarsening rate of precipitates is higher in 356 alloys than 319 alloys.
4. Cracks are found initiated from porosity in both 319 and 356 alloys. A large area of fractured Si and intermetallic particles is observed in 319 alloys, while debonded particles can be found on the crack path of 356 alloys.
5. The evolution of TMF behavior of 319 and 356 alloys was successfully simulated with a hysteresis energy model with promising accuracy.

CHAPTER 5 EFFECT OF MO ADDITION ON TMF PROPERTIES IN AL-SI CAST ALLOYS

Mo, as a dispersoid former element, can form a considerable amount of thermal stable dispersoids. During solution treatment of cast Al-Si alloys, Mo can form coherent α -Al-(Fe, Mo)-Si dispersoids in the interdendritic region of Al matrix, which are thermally stable after longtime exposure under elevated temperature and then retain their strengthening effect [8].

In this chapter, a certain amount of Mo (0.3 wt.%) was added into 319 and 356 alloys, named 319M and 356M respectively, and TMF tests under the same OP-TMF loading condition with 319 and 356 base alloys were performed on Mo-containing alloys. The TMF behavior and microstructure change between Mo-containing alloys and base alloys are discussed.

5.1 TMF behavior with Mo addition

5.1.1 Cyclic stress-strain behavior

Figure 5.1 shows the stress-strain hysteresis loops comparison of 319 and 319M alloy under different strain amplitudes of OP-TMF loading. Generally, the asymmetrical hysteresis loops and tensile mean stress can be seen in all strain amplitudes in 319 base alloy and 319M alloy. Cyclic softening behavior also can be found during TMF under various strain amplitude.

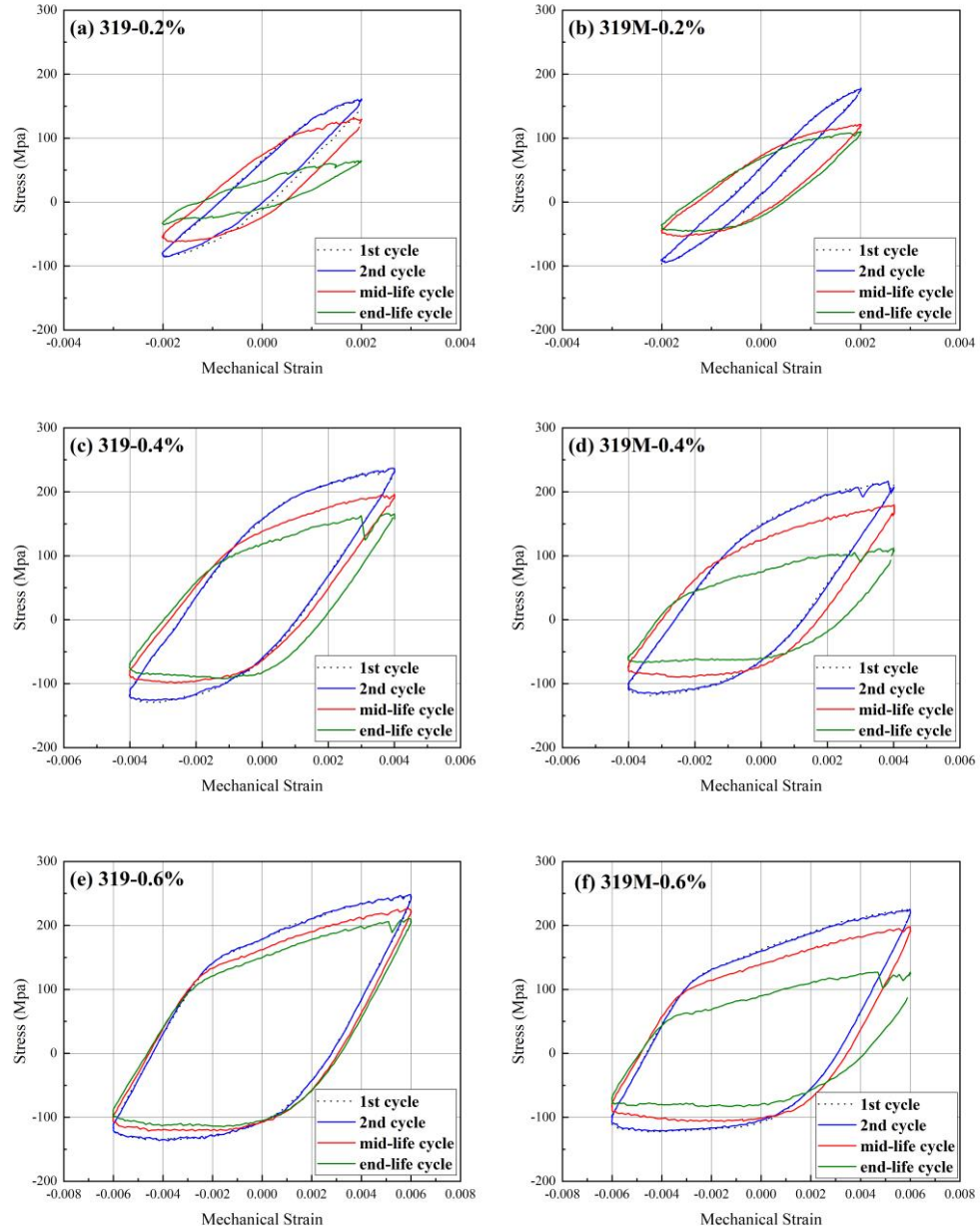


Figure 5.1 Stress-strain hysteresis loops under OP-TMF loading conditions of 319 and 319M alloy.

(a) 319-0.2%, (b) 319M-0.2%, (c) 319-0.4%, (d) 319M-0.4%, (e) 319-0.6% and (f) 319M-0.6%.

© Shuai Wang, 2021

Figure 5.2 shows the stress-strain hysteresis loops comparison of 356 and 356M alloy under different strain amplitudes of OP-TMF loading. Asymmetrical hysteresis loops, tensile mean stress, and cyclic softening behavior can also be observed in 356 and 356M alloy.

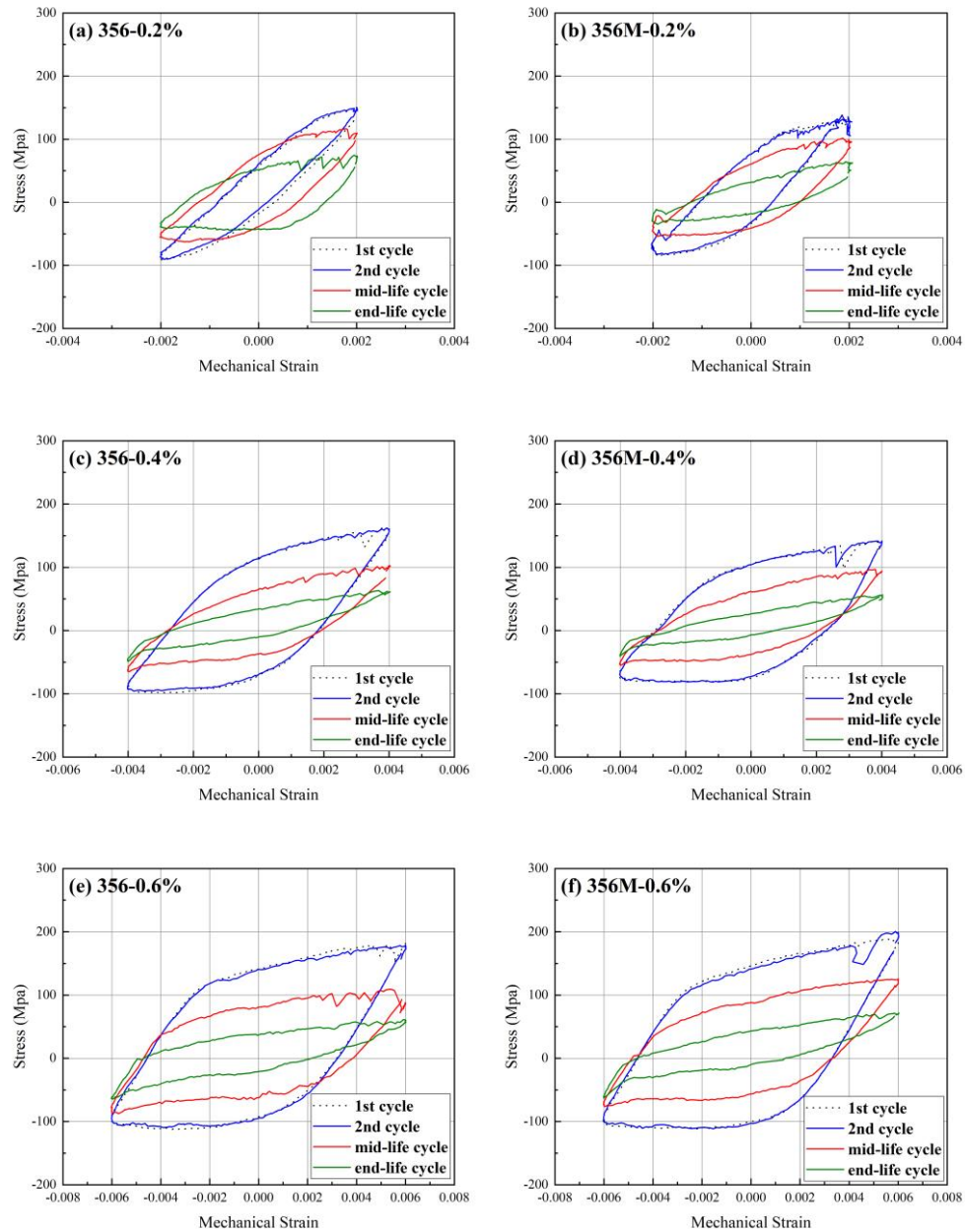


Figure 5.2 Stress-strain hysteresis loops under OP-TMF loading conditions of 356 and 356M alloy.

(a) 356-0.2%, (b) 356M-0.2%, (c) 356-0.4%, (d) 356M-0.4%, (e) 356-0.6% and (f) 356M-0.6%.

Figure 5.3 and Figure 5.4 show the cyclic stress evolution with fatigue cycles at different strain amplitude for 319/319M alloy and 356/356M alloy, respectively. In general, all tested samples show cyclic softening behavior at all strain amplitudes.

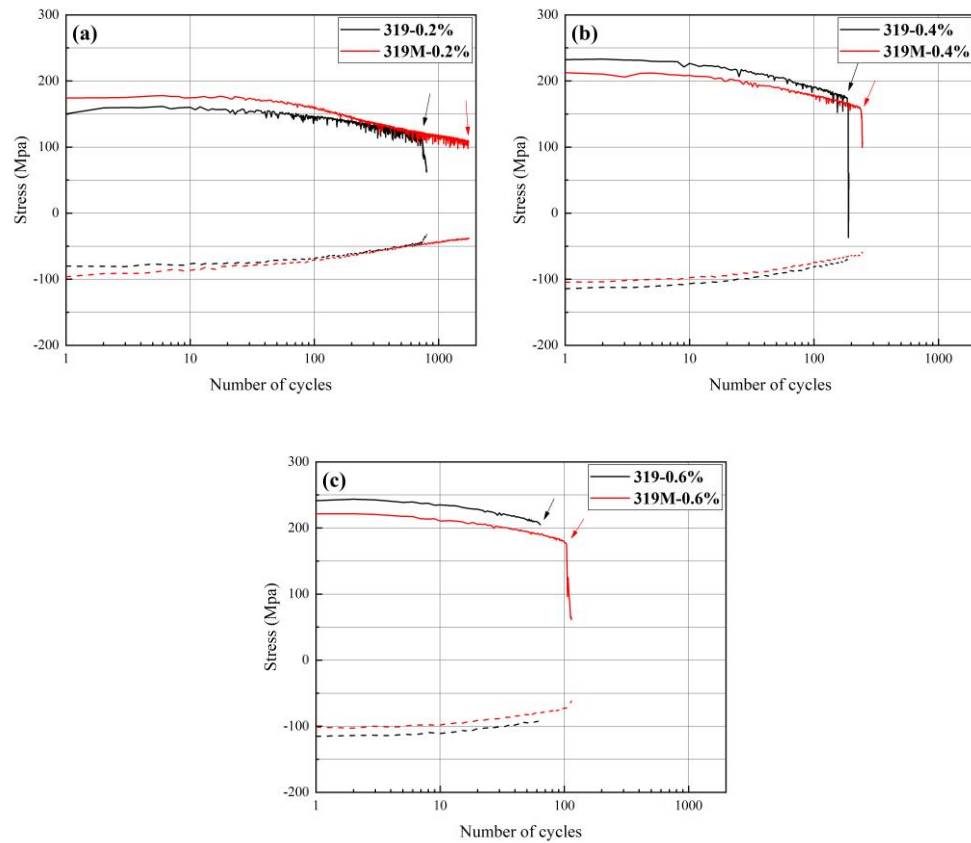


Figure 5.3 The evolution of maximum and minimum stress at different strain amplitude of 319 and 319M alloy, (a) 0.2%, (b) 0.4% and (c) 0.6%. © Shuai Wang, 2021

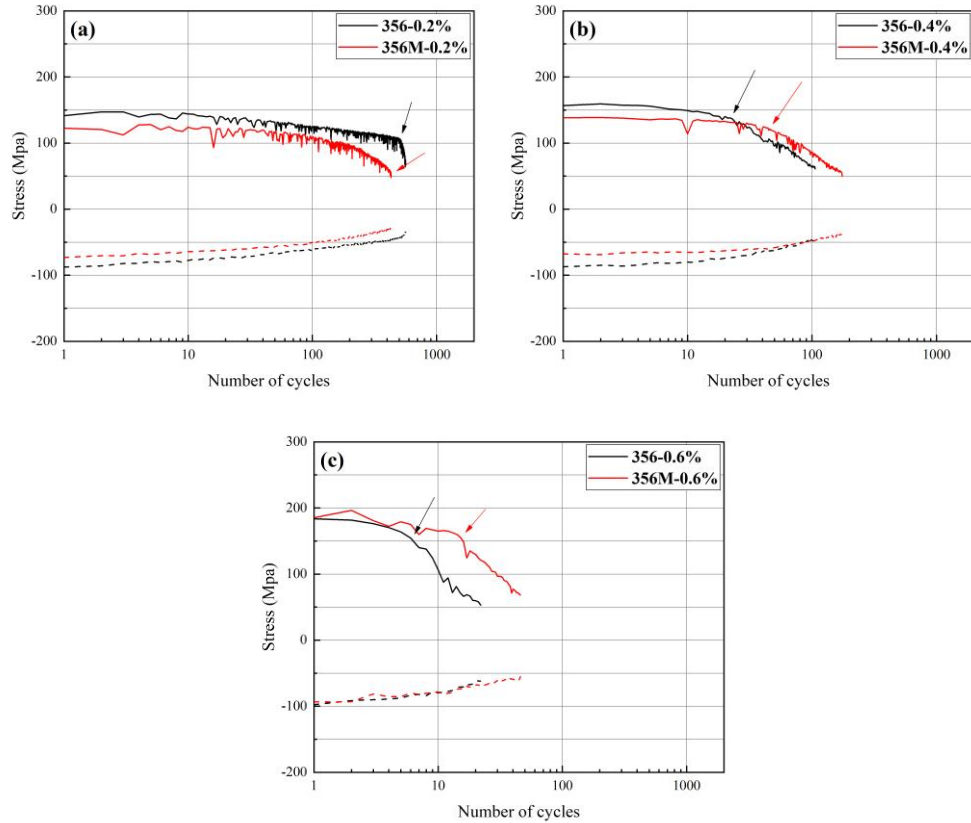


Figure 5.4 The evolution of maximum and minimum stress at different strain amplitude of 356 and 356M alloy, (a) 0.2%, (b) 0.4% and (c) 0.6%. © Shuai Wang, 2021

Many researchers have reported the strengthening effect of Mo in Al-Si alloy at ambient and elevated temperature [8-10, 43], but previous results from Figure 5.3 and Figure 5.4 show lower initial tensile stress of Mo-addition alloys than base alloys in few strain amplitudes, such as 319 and 319M alloys at 0.4% and 0.6% strain amplitude. This may attribute to the different times that samples took for zero-force adjustment before the TMF test start. During the zero-force adjustment process, the thermal strain was applied to test samples, which the temperature range is the same as the temperature field during the TMF test (60-300°C). The longer time sample used for the pre-test indicated a longer time for cyclic aging. The detailed pre-test time (PT) and initial tensile stress (ITS) from Figure 5.3 and Figure 5.4 are listed in

Table 5.1. It can be seen that the initial tensile stress increases as the strain amplitude increase for all Mo-free and Mo-addition alloys. Samples under certain strain amplitude which have higher initial tensile stress spend less time for pre-test, whether is Mo-free alloy or Mo-addition alloy. The cyclic aging during pre-test affects the precipitates, coarsening of main strengthening precipitates decreases the strength of the alloy. Similar results are reported by Zamani that the hardness of Mo-modified Al-Si alloy drastically decreased irrespective to Mo level when the alloy was exposed at 250°C for 48h as the primary strengthening precipitates (such as Al₂Cu and Mg₂Si) are coarsened [47].

Table 5.1 Pre-test time (PT) and initial tensile stress (ITS) of Mo-free and Mo-addition alloys at various strain.

	319		319M		356		356M	
Strain	PT(s)	ITS(MPa)	PT(s)	ITS(MPa)	PT(s)	ITS(MPa)	PT(s)	ITS(MPa)
0.2%	4969	150.14	4638	174.42	4638	142.93	6624	122.5
0.4%	4307	232.44	4969	212.6	5962	156.61	12582	138.48
0.6%	5962	241.3	6624	221.48	4969	164.51	4638	186.83

The proportion of stage I in total TMF lifetime has been calculated and listed in Table 5.2. For 319M samples, due to the high stage I proportion of 319 base alloy, the improvement with Mo addition this phenomenon is not very obvious, only 10% increment of stage I at 0.2% strain amplitude while presenting 10% decrement at 0.6% strain amplitude. For 356M samples, there is 15% increment compared with 356 base alloy at 0.2% strain amplitude, 4% and 3% increment for 0.4% and 0.6% strain respectively. It can be seen that with Mo addition, 356M samples spend a longer time in stage I during TMF.

Table 5.2 Proportion of stage I in total TMF lifetime of 319 and 356 alloys at a different strain amplitude

Strain\Alloy	319	319M	356	356M
0.2%	90%	100%	85%	100%
0.4%	96%	96%	22%	26%
0.6%	100%	90%	27%	30%

5.1.2 Lifetime behavior

Figure 5.5 shows the relationship between strain amplitude and TMF lifetime of Mo-free and Mo-addition 319 and 356 alloys, respectively. Generally, all samples have decreased fatigue life with increasing strain amplitude. For 319 alloys, 319M shows higher TMF life than 319 base alloy among all tested strain amplitude, the increment on TMF life decrease with strain amplitude increasing. For 356 alloys, Mo-addition alloy shows lower TMF life than 356 base alloy at 0.2% strain amplitude. At 0.4% strain amplitude, 356 and 356M alloys have similar results on maximum TMF life and average TMF life, while the minimum result is lower for 356M alloy. 356M shows better TMF life than 356 base alloy at 0.6% strain amplitude.

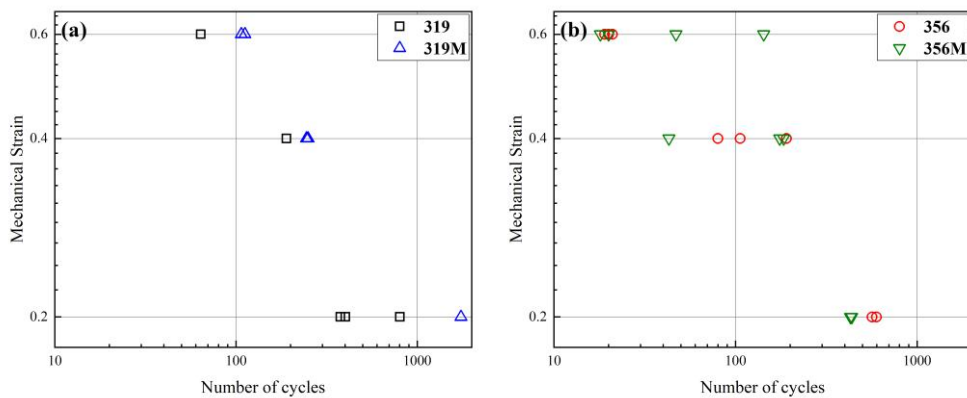


Figure 5.5 Mechanical strain amplitude vs number of cycles of (a) 319/319M alloy, and (b) 356/356M

alloy. © Shuai Wang, 2021

5.1.3 Microstructure observation

5.1.3.1 Initial microstructure

The microstructure of 319M and 356M alloys is investigated before and after TMF tests and compared with Mo-free alloys. Low-magnification images are obtained by optical microscope. Figure 5.6 shows the microstructure before TMF of 319M and 356M alloy. Similar microstructure as 319 and 356 base alloy can be seen in 319M and 356M samples. By EDS analysis identification, Mo can be found in Fe-bearing intermetallics as α -Al-(Fe, Mn, Mo)-Si phase with Chinese script morphology, no other Fe-bearing phase observed and no Mo detected in the α -Al matrix for both 319M and 356M alloys.

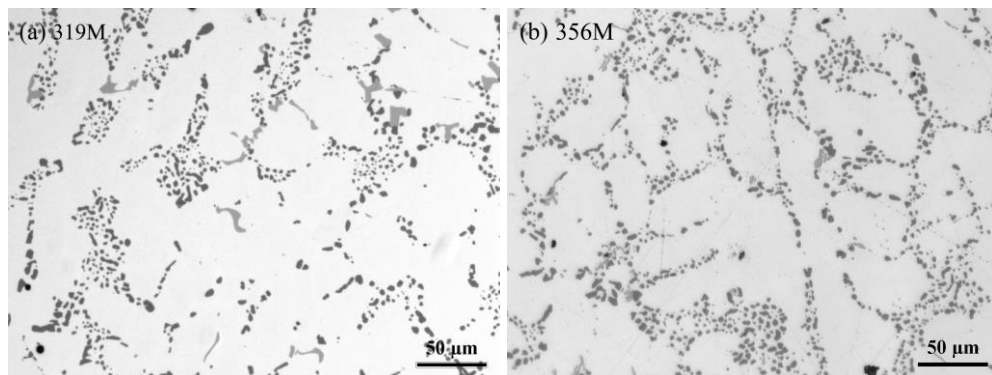


Figure 5.6 Microstructure before TMF of (a) 319M alloy and (b) 356M alloy. © Shuai Wang, 2021

The properties of intermetallic phases have been investigated by analysis software and are listed in Table 5.3. Compared with Mo-free alloys, the microstructure with Mo-addition has no significant change before TMF due to the limited content of Mo. 319 alloy is more likely to have microstructure damage during TMF due to its higher intermetallics content.

Table 5.3 Analysis results of microstructure of 319 and 356 alloy before TMF

	319 alloy	319M alloy	356 alloy	356M alloy
Morphology of eutectic Si	Lamellar /globular	Lamellar /globular	Globular /granular	Globular /granular
Spher.Diam of eutectic Si	4.0 μ m	3.8 μ m	3.5 μ m	3.8 μ m
Area fraction of other IMCs	1.6%	2.0%	0.8%	1.1%

5.1.3.2 Evolution of precipitation during TMF

Nano-sized microstructure of 319M and 356M alloys were investigated by TEM before and after TMF tests. Figure 5.7 shows the observation results of 319M and 356M alloys. θ' -Al₂Cu and β' -Mg₂Si precipitates are recognized as major precipitates in 319M and 356M alloys respectively. Mo content can only be detected from α -Al-(Fe, Mn, Mo)-Si dispersoids in Al matrix in both 319M and 356M alloys. EDS analysis results for the Al matrix and Mo-containing dispersoids of both 319M and 356M alloys are shown in Figure 5.8. Dispersoids of Al-(Fe, Mn, Mo)-Si are detected in both 319 and 356 alloys.

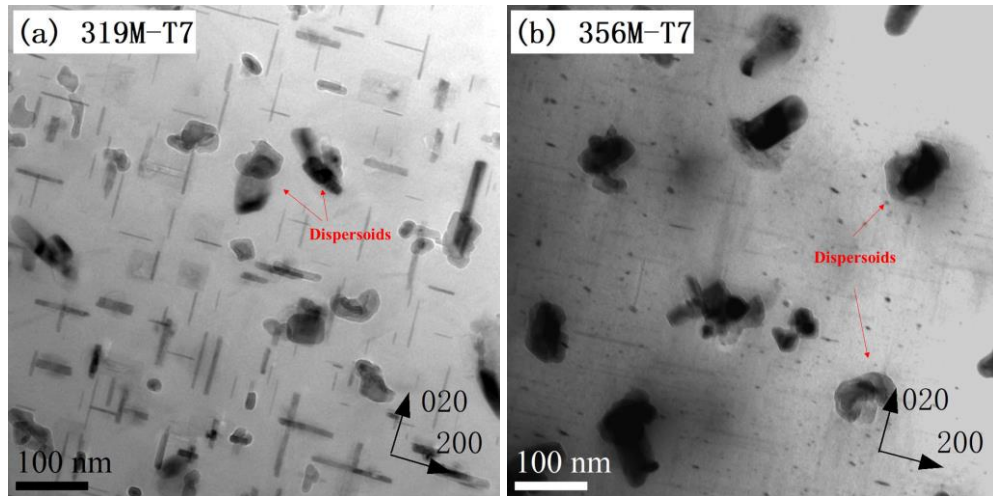


Figure 5.7 TEM microstructure before TMF of (a) 319M alloy and (b) 356M alloy.

© Shuai Wang, 2021

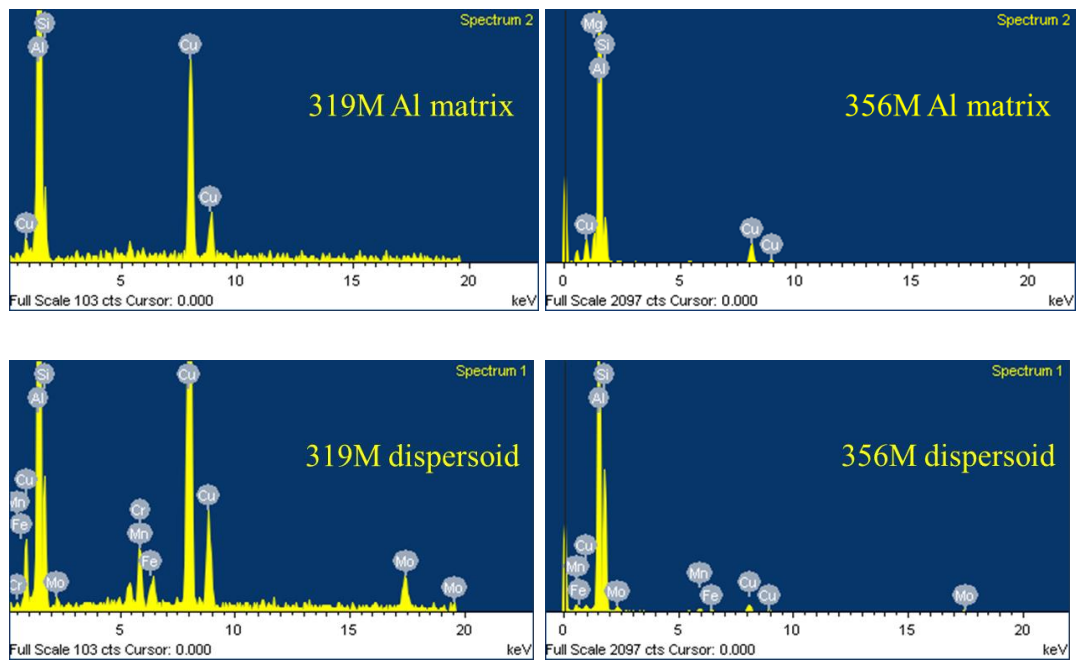


Figure 5.8 EDS spectrums confirm the composition of Al matrix and dispersoids of 319M and 356M

alloys. © Shuai Wang, 2021

Figure 5.9 shows the precipitates of 319M alloy after various strain amplitudes of TMF tests. Similar to 319 base alloy, the major strengthening precipitate θ' -Al₂Cu phase was coarsened and decreased in number after TMF.

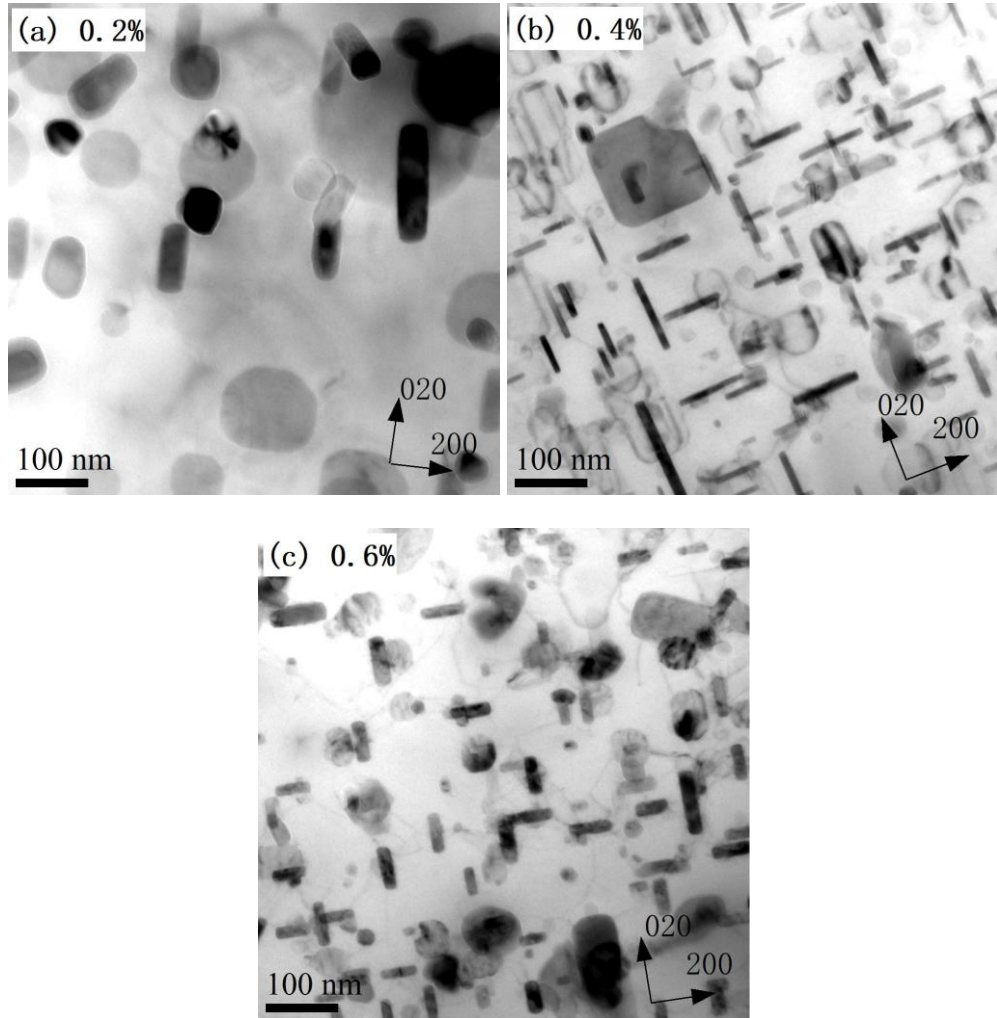


Figure 5.9 Precipitates microstructure of 319M alloy after TMF, the loading direction is perpendicular to the image, (a) 0.2%, (b) 0.4% and (c) 0.6%. © Shuai Wang, 2021

Figure 5.10 shows the precipitates of 356M alloy after various strain amplitudes of TMF tests. Rod-like β' - Mg_2Si phase and Q- $\text{Al}_5\text{Mg}_8\text{Cu}_2\text{Si}_6$ phase can be detected from the samples after the TMF test.

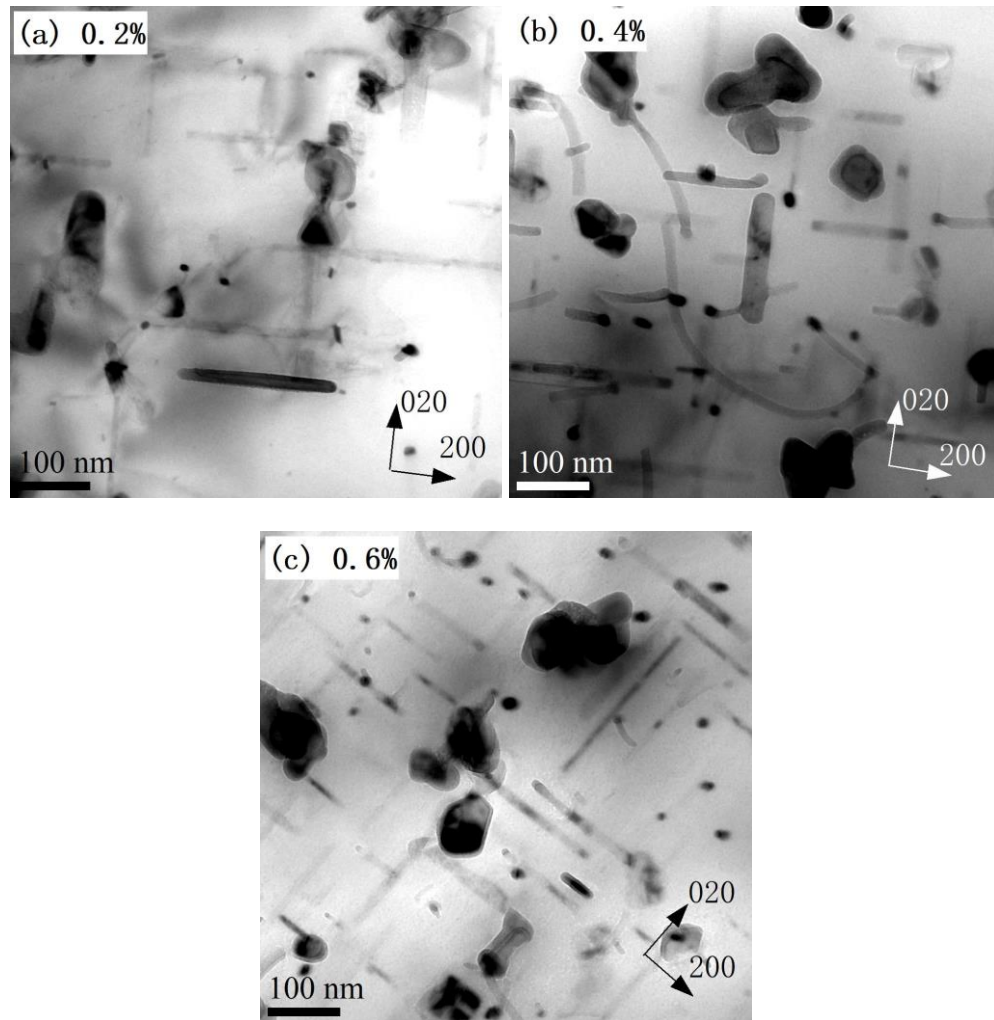


Figure 5.10 Precipitates microstructure of 356M alloy after TMF, the loading direction is perpendicular to the image, (a) 0.2%, (b) 0.4% and (c) 0.6%. © Shuai Wang, 2021

The precipitates parameters of 319M and 356M alloys are summarized and listed together with 319 and 356 base alloys in Table 5.4 for comparison. Precipitates in 319M and

356M alloys before TMF have larger sizes and lower number density compared with 319 and 356 base alloys. During TMF, alloys with Mo-addition presents precipitates coarsening behavior and significantly decrement in number density.

Table 5.4 Parameters of precipitates of Mo-free and Mo-addition alloys

Alloy	Status	Precipitates length (nm)	Precipitates width (nm)	Number density (μm^{-1})
319	Before TMF	24.05	2.14	4451.2
	After 0.2%	57.94	6.04	501.4
	After 0.4%	41.97	4.99	789.8
	After 0.6%	40.07	9.03	690.6
319M	Before TMF	33.75	2.71	3635.3
	After 0.2%	65.64	18.96	92.87
	After 0.4%	45.12	5.47	742.4
	After 0.6%	33.9	9.79	406.6
356	Before TMF	35.01	1.38	19144.8
	After 0.2%	165.54	7.46	191.1
	After 0.4%	102.38	7.29	253.7
	After 0.6%	102.4	6.28	394.0
356M	Before TMF	42.77	1.85	11946.9
	After 0.2%	125.33	5.32	188.07
	After 0.4%	129.88	6.21	102.83
	After 0.6%	87.85	6.44	441.38

Similar as precipitates, the parameters of dispersoids for both 319 and 356 alloys are also summarized in Table 5.5. As seen from the Table 5.5, the average size of dispersoids before TMF test are similar for both 319 and 356 alloys. After TMF test with various strain amplitudes, the average size of dispersoids slightly increased. The number density of

dispersoids of 319 and 356 base alloys slightly increased with Mo addition, and no significant difference on number density of dispersoids for the condition before and after TMF test.

Table 5.5 Parameters of dispersoids of Mo-free and Mo-addition alloys

Alloy	Status	Dispersoids average size (nm)	Number density (μm^{-1})
319	Before TMF	143	3.23
	After 0.2%	162	3.24
	After 0.4%	149	3.29
	After 0.6%	149	3.21
319M	Before TMF	145	3.37
	After 0.2%	168	3.35
	After 0.4%	153	3.32
	After 0.6%	151	3.37
356	Before TMF	139	3.21
	After 0.2%	156	3.26
	After 0.4%	140	3.23
	After 0.6%	142	3.23
356M	Before TMF	143	3.30
	After 0.2%	146	3.39
	After 0.4%	144	3.34
	After 0.6%	140	3.33

By using the LSW equation from Equation 2, the coarsening rate of 319M and 356M alloys are calculated and compared with 319 and 356 base alloys in Table 5.6. Generally, the k value increase with increased strain amplitude. With Mo-addition, 319M and 356M alloys show lower k value than their base alloys in most tested strain amplitude.

Table 5.6 Coarsening rate constant k of Mo-free and Mo-addition alloys after OP-TMF

k	$t^{1/2}$ law results				$t^{1/3}$ law results			
	319	319M	356	356M	319	319M	356	356M
After 0.2%	3.45	1.81	43.85	34.75	224.62	139.97	7527.72	4529.24
After 0.4%	6.22	3.66	87.32	92.02	381.21	218.16	9719.85	12397.96
After 0.6%	16.05	0.08	463.01	147.94	788.03	4.50	51546.52	13978.25

As previously concluded, due to the coarsening behavior of precipitates, the strengthening effect decreased during TMF. With Mo addition, a substantial amount of nano-scale Al(Fe, Mo)Si dispersoids precipitated during solution treatment, which is thermally stable after longtime exposure under elevated temperature. Besides, due to the opposite partitioning behavior of Mo and Mn, the combination of Mo and Mn leads to a more uniform distribution of dispersoids. The number of dispersoids per unit area increases while the average dispersoids size decreases [9]. The presence of dispersoids in Mo-addition alloys act as a dislocation barrier during fatigue, in which the dislocations act as solute atoms carrier during TMF, resulting in a lower coarsening rate.

5.1.3.3 Fractography

The fracture surface of 319M and 356M alloys are examined by SEM, the overview of fractured samples of 319M and 356M alloys are plotted in Figure 5.11. As seen that cracks initiate from porosity inside or close to the specimen surface, especially obvious in 356M alloy.

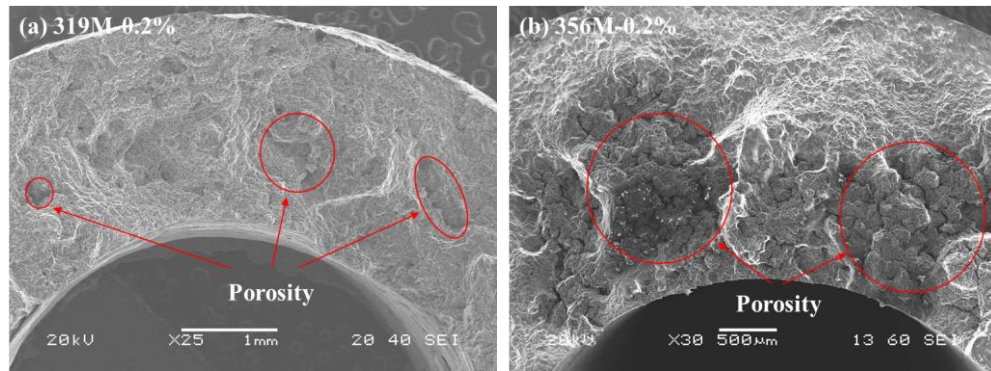


Figure 5.11 Overall view of fracture surface after 0.2% TMF test (a) 319M alloy and (b) 356M alloy.

© Shuai Wang, 2021

Figure 5.12 presents the fracture morphology in the crack propagation area of 319M and 356M alloys. From the observation results, Mo-addition has no change on the crack growth mechanism of 319 and 356 alloys, as Fe-bearing intermetallics and fractured eutectic Si can be observed in 319M fracture samples. The crack path through the α -Al matrix with limited numbers of eutectic Si and intermetallic particles can be found in 356M alloy fracture samples.

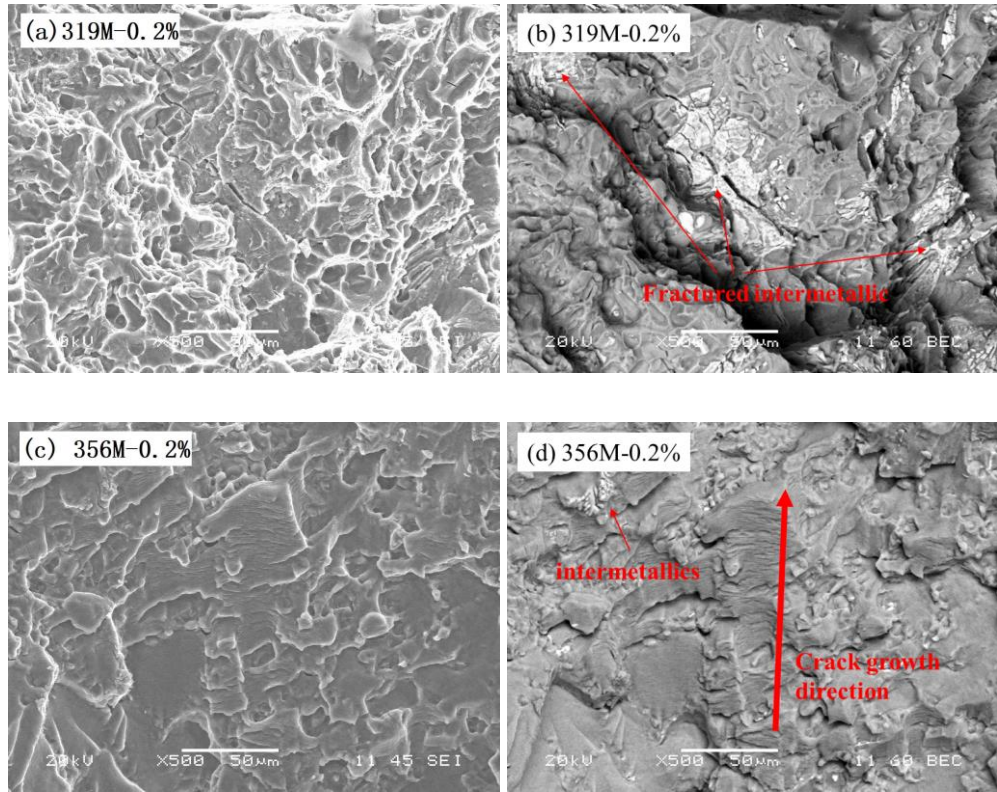


Figure 5.12 Fractography and BSE micrograph of fractured specimen after 0.2% TMF test. (a, b) 319M alloy and (c, d) 356M alloy. © Shuai Wang, 2021

Fatigue striations show a stable crack growth region, each striation is produced by a single fatigue cycle and represents the position of advancing crack during the fatigue process. Figure 5.13 shows the fatigue striation at 0.4% strain amplitude of 356 and 356M alloys. As seen, the fatigue striation spacing of 356Mo is smaller than 356 base alloy, which is attributed to homogenized plastic deformation with the presence of Mo-dispersoids.

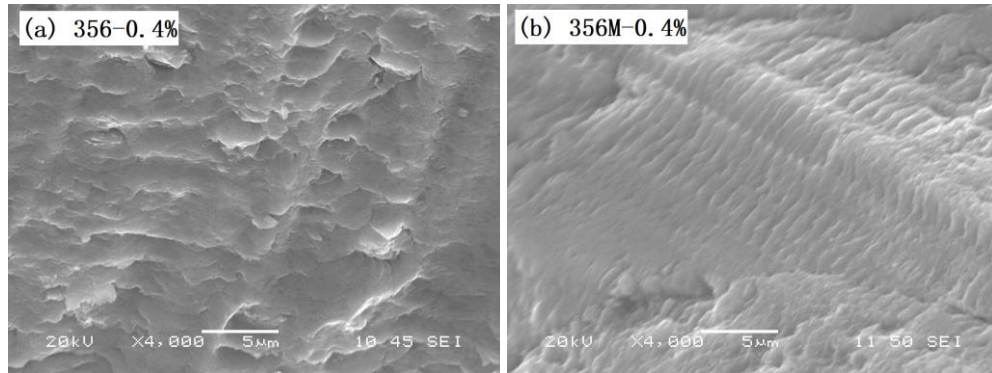


Figure 5.13 Fatigue striations under 4000x magnification in (a) 356-0.4% and (b) 356M-0.4%.

© Shuai Wang, 2021

During fatigue, crack tends to grow from persistent slip bands. With Mo addition, dispersoids act as dislocation barriers and uniform slip distribution, which can delay the initiation of fatigue crack and extend fatigue life. However, the presence of porosity helps the crack initiation process due to stress concentration, which results in a detrimental effect on fatigue behavior and fatigue lifetime. Therefore, the improvement provided by Mo-dispersoids has been neutralized.

5.2 TMF lifetime parameters

As previously introduced, the hysteresis energy model can be used for evaluating the TMF properties by involving both strain and stress amplitudes. Alloys properties with chemical composition adjustment can be evaluated after TMF tests. Figure 5.14 shows the hysteresis energy evolution with TMF cycles for 319M and 356M alloy. The hysteresis energy of Mo-addition alloys presents cyclic stability for most of their TMF lifetime.

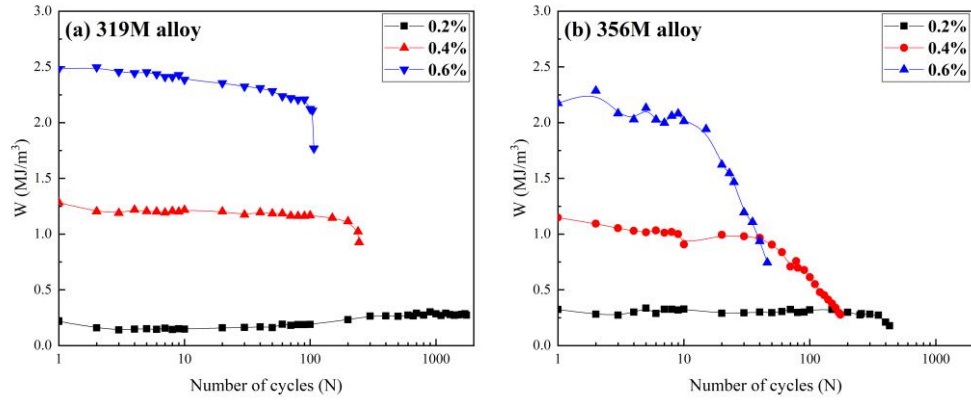


Figure 5.14 Hysteresis energy as a function of number of cycles for (a) 319M alloy and (b) 356M alloy. © Shuai Wang, 2021

Based on the hysteresis energy model of Equation 4, the value of fatigue parameters for 319M and 356M alloys are compared with 319 and 356 base alloys and listed in Table 5.7 and the TMF behavior expressed by energy model equations are plotted in Figure 5.15. As seen below, with Mo addition, both 319M and 356M alloys present a lower W_0 value and a higher β value. Besides, the shape factor C was also found slightly increased, which contributes to homogenized plastic deformation with Mo addition. All the TMF results fall within the 2 times scatter band based on the energy model, as shown in Figure 5.15, which indicates the energy model can be used to characterize the TMF behavior of different alloys with promising accuracy. From Figure 5.15, the strengthening effect of Mo-addition on TMF lifetime can be seen. The increment of TMF lifetime with Mo-addition decrease with increasing hysteresis energy, indicating Mo-addition with better TMF lifetime strengthening effect at low strain amplitude such as 0.2%. 319 alloys have better TMF life increment than 356 alloys with Mo-addition.

Table 5.7 Value of parameters calculated by hysteresis energy model.

	W_0	β	C
319 alloy	167.43	0.98	0.91
319M alloy	101.95	1.23	0.92
356 alloy	5.06	2.39	0.84
356M alloy	4.82	2.55	0.93

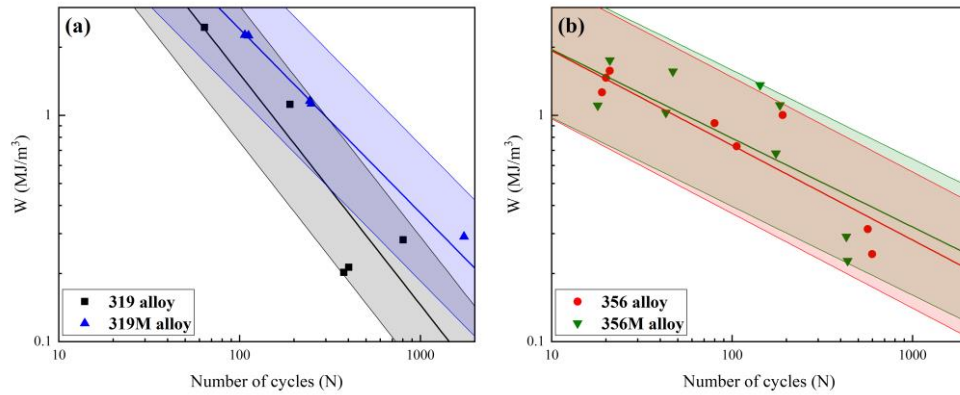


Figure 5.15 TMF lifetime results and hysteresis energy model fitting results for (a) 319 and 319M alloy, (b) 356 and 356M alloy. © Shuai Wang, 2021

5.3 Summary

In this chapter, the effect of Mo addition on TMF properties of 319 and 356 alloys is investigated. Based on the results and discussion, the following conclusion can be drawn:

1. Similar cyclic softening behavior and asymmetrical hysteresis loop with tensile mean stress can be found in 319M and 356M alloys.
2. With Mo addition, 319M alloy show longer TMF life than 319 base alloy in all tested strain amplitudes. While 356M alloy only shows longer TMF life than 356 base alloy at 0.4% and 0.6% strain amplitudes.
3. Mo addition shows a decrement in coarsening rate of precipitates. Mo-addition forms high-density thermally stable dispersoids in the α -Al matrix, which act as dislocation

barriers and homogenize plastic deformation, resulting in lower fatigue crack growth rate and longer fatigue lifetime. However, the presence of porosity has a detrimental effect on fatigue lifetime for early crack initiation.

4. The simulated TMF results by hysteresis energy model present the effect of Mo-addition on TMF behavior of 319 and 356 alloys. The strengthening effect of Mo is more obvious at low strain amplitudes.

CHAPTER 6 CONCLUSIONS

In the present work, the TMF behavior under various strain amplitudes (0.2%-0.6%) and temperature ranges (60°C-300°C) loading conditions for two typical Al-Si cast alloys, 319 (Al-Si-Cu) alloy and 356 (Al-Si-Mg) alloy have been investigated. Meanwhile, the effect of Mo addition on their TMF properties is also investigated. Based on all the results and discussions, the conclusion can be drawn as two parts below:

Part I: TMF behavior of 319 and 356 alloys

1. Both 319 and 356 alloys show cyclic softening behavior during TMF at all tested strain amplitudes, and asymmetrical hysteresis loops with tensile mean stress also can be found in both 319 and 356 alloys.
2. 319 alloy shows similar TMF life with 356 alloys at 0.2% and 0.4%, but longer TMF life at 0.6% strain amplitude.
3. After TMF, the number density of precipitates in both 319 and 356 alloys shows a significant decrease, indicating their coarsening during TMF. However, the coarsening rate of precipitates is higher in 356 alloys than 319 alloys.
4. Cracks are found initiated from porosity in both 319 and 356 alloys. A large area of fractured Si and intermetallic particles is observed in 319 alloys, while debonded particles can be found on the crack path of 356 alloys.
5. The evolution of TMF behavior of 319 and 356 alloys was successfully simulated with an energy model with promising accuracy.

Part II: Influence of Mo addition on TMF behaviors

1. Similar cyclic softening behavior and asymmetrical hysteresis loops with tensile mean stress can be found in 319M and 356M alloys.
2. With Mo addition, 319M alloy show longer TMF life than 319 base alloy in all tested strain amplitudes. While 356M alloy only shows longer TMF life than 356 base alloy at 0.4% and 0.6% strain amplitudes.
3. Mo addition shows a decrement in coarsening rate of precipitates. Mo- dispersoids act as dislocation barriers and homogenize plastic deformation, resulting in lower fatigue crack growth rate and longer fatigue lifetime. However, the presence of porosity has a detrimental effect on fatigue lifetime for early crack initiation.
4. The simulated TMF results by hysteresis energy model present the effect of Mo-addition on TMF behavior of 319 and 356 alloys. The strengthening effect of Mo is more obvious at low strain amplitudes.

CHAPTER 7 RECOMMENDATIONS

According to the present work, the following recommendations can be made:

1. According to previous results and discussion, the presence of porosity helps crack initiation which can lead to a detrimental effect on TMF lifetime. Therefore, the casting procedures need improvement to reduce the volume of porosity.
2. To study the evolution of microstructure of different alloys during TMF, TMF tests with an interruption at fixed cycles before final failure are recommended for future work.
3. In this project, the energy model was only used for characterizing the TMF behavior of different alloys. Further study can focus on the energy model for TMF lifetime prediction by involving more parameters such as temperature range and/or mechanical strain amplitudes.

REFERENCES

- [1] C. Samaras and K. Meisterling, "Life cycle assessment of greenhouse gas emissions from plug-in hybrid vehicles: implications for policy," éd: ACS Publications, 2008.
- [2] G. Cole and A. Sherman, "Light weight materials for automotive applications," *Materials characterization*, vol. 35, no. 1, pp. 3-9, 1995.
- [3] M. Javidani and D. Larouche, "Application of cast Al–Si alloys in internal combustion engine components," *International Materials Reviews*, vol. 59, no. 3, pp. 132-158, 2014.
- [4] R. Neu and H. Sehitoglu, "Thermomechanical fatigue, oxidation, and creep: Part I. Damage mechanisms," *Metallurgical transactions A*, vol. 20, no. 9, pp. 1755-1767, 1989.
- [5] R. Neu and H. Sehitoglu, "Thermomechanical fatigue, oxidation, and creep: Part II. Life prediction," *Metallurgical transactions A*, vol. 20, no. 9, pp. 1769-1783, 1989.
- [6] M. Whittaker, R. Lancaster, W. Harrison, C. Pretty, and S. Williams, "An Empirical Approach to Correlating Thermo-Mechanical Fatigue Behaviour of a Polycrystalline Ni-Base Superalloy," *Materials*, vol. 6, pp. 5275-5290, 11/01 2013.
- [7] G. Han, J. Yu, X. Sun, and Z. Hu, "Thermo-mechanical fatigue behavior of a single crystal nickel-based superalloy," *Materials Science and Engineering: A*, vol. 528, no. 19-20, pp. 6217-6224, 2011.
- [8] A. Farkoosh, X. G. Chen, and M. Pekguleryuz, "Dispersoid strengthening of a high temperature Al–Si–Cu–Mg alloy via Mo addition," *Materials Science and Engineering: A*, vol. 620, pp. 181-189, 2015.
- [9] A. Farkoosh, X. G. Chen, and M. Pekguleryuz, "Interaction between molybdenum and manganese to form effective dispersoids in an Al–Si–Cu–Mg alloy and their influence on creep resistance," *Materials Science and Engineering: A*, vol. 627, pp. 127-138, 2015.
- [10] S. Chen, K. Liu, and X. G. Chen, "Precipitation behavior of dispersoids and elevated-temperature properties in Al–Si–Mg foundry alloy with Mo addition," *Journal of Materials Research*, vol. 34, no. 18, pp. 3071-3081, 2019/09/01 2019.
- [11] M. Garat and G. Laslaz, "07-002 Improved Aluminium Alloys for Common Rail Diesel Cylinder Heads," *TRANSACTIONS-AMERICAN FOUNDRYMENS SOCIETY*, vol. 115, p. 89, 2007.
- [12] R. Chuimert and M. Garat, présenté à 3rd Int. Symp. Aluminium Automobile, Dusseldorf, 1988, pp. 154-159.
- [13] F. Feikus, "Optimization of Al-Si cast alloys for cylinder head applications," *American Foundrymen's Society, Inc, Transactions of the American Foundrymen's Society*, vol. 106, pp. 225-231, 1998.
- [14] G. Laslaz and M. Garat, "US Patent, 0224145 Al," 2005.
- [15] J. G. Kaufman, *Introduction to aluminum alloys and tempers*. ASM international, 2000.
- [16] A. H. Committee, "Heat treating," *Volume*, vol. 4, pp. 1848-1960, 1991.
- [17] M. LF, "Mondolfo, Aluminium alloys: Structure and Properties," éd: London, Butterworth &Co (Publishers) Ltd, 1976.
- [18] M. Makhlouf and H. Guthy, "The aluminum–silicon eutectic reaction: mechanisms and crystallography," *Journal of light metals*, vol. 1, no. 4, pp. 199-218, 2001.

- [19] M. Tash, F. H. Samuel, F. Mucciardi, and H. W. Doty, "Effect of metallurgical parameters on the hardness and microstructural characterization of as-cast and heat-treated 356 and 319 aluminum alloys," *Materials Science and Engineering: A*, vol. 443, no. 1, pp. 185-201, 2007/01/15/ 2007.
- [20] K. Gall, N. Yang, M. Horstemeyer, D. L. McDowell, and J. Fan, "The debonding and fracture of Si particles during the fatigue of a cast Al-Si alloy," *Metallurgical and Materials Transactions A*, vol. 30, no. 12, pp. 3079-3088, 1999.
- [21] J. Luft, T. Beck, and D. Löhe, "Lifetime and damage behavior of a cast aluminum alloy under TMF and superimposed TMF/HCF loading."
- [22] A. Hany, "Influence of metallurgical parameters on the mechanical properties and quality indices of Al-Si-Cu-Mg and Al-Si-Mg casting alloys," PhD thesis, Université du Québec à Chicoutimi, Québec, Canada, 2010.
- [23] O. Elsebaie, *Effects of strontium-modification, iron-based intermetallics and aging conditions on the impact toughness of Al-(6-11)% Si alloys*. Université du Québec à Chicoutimi, 2010.
- [24] S. Murali, K. S. Raman, and K. S. S. Murthy, "Effect of magnesium, iron (impurity) and solidification rates on the fracture toughness of Al 7Si 0.3Mg casting alloy," *Materials Science and Engineering: A*, vol. 151, no. 1, pp. 1-10, 1992/04/15/ 1992.
- [25] K. T. Kashyap, S. Murali, K. S. Raman, and K. S. S. Murthy, "Casting and heat treatment variables of Al-7Si-Mg alloy," *Materials Science and Technology*, vol. 9, no. 3, pp. 189-204, 1993/03/01 1993.
- [26] M. F. Ibrahim, E. M. Elgallad, S. Valtierra, H. W. Doty, and F. H. Samuel, "Metallurgical Parameters Controlling the Eutectic Silicon Characteristics in Be-Treated Al-Si-Mg Alloys," (en eng), *Materials (Basel, Switzerland)*, vol. 9, no. 2, p. 78, 2016.
- [27] J. A. Taylor, D. H. StJohn, J. Barresi, and M. J. Couper, "Influence of Mg Content on the Microstructure and Solid Solution Chemistry of Al-7%Si-Mg Casting Alloys During Solution Treatment," *Materials Science Forum*, vol. 331-337, pp. 277-282, 2000.
- [28] G. A. Edwards, K. Stiller, G. L. Dunlop, and M. J. Couper, "The precipitation sequence in Al-Mg-Si alloys," *Acta Materialia*, vol. 46, no. 11, pp. 3893-3904, 1998/07/01/ 1998.
- [29] D. L. Zhang, "Precipitation of excess silicon during heat treatment of cast Al-7wt% Si-0.4 wt% Mg alloy," *Dans Materials Science Forum*, 1996, vol. 217, pp. 771-776: Trans Tech Publ.
- [30] J. F. Hernández Paz, "Heat treatment and precipitation in A356 aluminum alloy," 2003.
- [31] A. I. H. Committee, *Metals Handbook: Casting*. ASM International, 1988.
- [32] M. Misra and K. Oswalt, "Aging characteristics of titanium-refined A356 and A357 aluminum castings," *AFS Transactions*, vol. 90, pp. 1-10, 1982.
- [33] D. A. Porter and K. E. Easterling, *Phase transformations in metals and alloys (revised reprint)*. CRC press, 2009.
- [34] S. Wang and M. Starink, "Precipitates and intermetallic phases in precipitation hardening Al-Cu-Mg-(Li) based alloys," *International Materials Reviews*, vol. 50, no. 4, pp. 193-215, 2005.
- [35] W. Stobbs and G. Purdy, "The elastic accommodation of semicoherent θ' in Al 4wt.% Cu alloy," *Acta Metallurgica*, vol. 26, no. 7, pp. 1069-1081, 1978.
- [36] S. Ringer and K. Hono, "Microstructural evolution and age hardening in aluminium alloys: atom probe field-ion microscopy and transmission electron microscopy studies," *Materials characterization*, vol. 44, no. 1-2, pp. 101-131, 2000.

- [37] V. Phillips, "Lattice resolution measurement of strain fields at Guinier-Preston zones in Al-3.0% Cu," *Acta Metallurgica*, vol. 21, no. 3, pp. 219-228, 1973.
- [38] J. Taylor, *The effect of iron in Al-Si casting alloys*. 2004.
- [39] S. S. Kumari, R. Pillai, and B. Pai, "A study on the structural, age hardening and mechanical characteristics of Mn and Ca added Al-7Si-0.3 Mg-0.6 Fe alloy," *Journal of alloys and compounds*, vol. 453, no. 1-2, pp. 167-173, 2008.
- [40] J. Y. Hwang, H. W. Doty, and M. J. Kaufman, "The effects of Mn additions on the microstructure and mechanical properties of Al-Si-Cu casting alloys," *Materials Science and Engineering: A*, vol. 488, no. 1, pp. 496-504, 2008/08/15/ 2008.
- [41] H. Y. Kim, S. W. Han, and H. M. Lee, "The influence of Mn and Cr on the tensile properties of A356-0.20 Fe alloy," *Materials Letters*, vol. 60, no. 15, pp. 1880-1883, 2006.
- [42] H. Y. Kim, T. Y. Park, S. W. Han, and H. M. Lee, "Effects of Mn on the crystal structure of α -Al(Mn,Fe)Si particles in A356 alloys," *Journal of Crystal Growth*, vol. 291, no. 1, pp. 207-211, 2006/05/15/ 2006.
- [43] L. Jin, K. Liu, and X. G. Chen, "Evolution of Fe-Rich Intermetallics in Al-Si-Cu 319 Cast Alloy with Various Fe, Mo, and Mn Contents," *Metallurgical and Materials Transactions B*, vol. 50, no. 4, pp. 1896-1907, 2019/08/01 2019.
- [44] M. Mahta, M. Emamy, A. Daman, A. Keyvani, and J. Campbell, "Precipitation of Fe rich intermetallics in Cr-and Co-modified A413 alloy," *International Journal of Cast Metals Research*, vol. 18, no. 2, pp. 73-79, 2005.
- [45] S. K. Shaha, F. Czerwinski, W. Kasprzak, J. Friedman, and D. L. Chen, "Ageing characteristics and high-temperature tensile properties of Al-Si-Cu-Mg alloys with micro-additions of Mo and Mn," *Materials Science and Engineering: A*, vol. 684, pp. 726-736, 2017/01/27/ 2017.
- [46] L. Jin, K. Liu, and X. G. Chen, "Evolution of dispersoids and their effects on elevated-temperature strength and creep resistance in Al-Si-Cu 319 cast alloys with Mn and Mo additions," *Materials Science and Engineering: A*, vol. 770, p. 138554, 2020/01/07/ 2020.
- [47] M. Zamani, S. Toschi, A. Morri, L. Ceschini, and S. Seifeddine, "Effect of Mo Addition on Room and High Temperature Tensile Behavior of Al-Si-Cu-Mg Alloy in As-Cast and Heat-Treated Conditions," *Advanced Materials Research*, vol. 1155, pp. 71-79, 2019.
- [48] M. Djurdjevic, T. Stockwell, and J. Sokolowski, "The effect of strontium on the microstructure of the aluminium-silicon and aluminium-copper eutectics in the 319 aluminium alloy," *International Journal of Cast Metals Research*, vol. 12, no. 2, pp. 67-73, 1999.
- [49] J. G. Kaufman and E. L. Rooy, *Aluminum alloy castings: properties, processes, and applications*. Asm International, 2004.
- [50] E. Cerri, E. Evangelista, S. Spigarelli, P. Cavaliere, and F. DeRiccardis, "Effects of thermal treatments on microstructure and mechanical properties in a thixocast 319 aluminum alloy," *Materials Science and Engineering: A*, vol. 284, no. 1-2, pp. 254-260, 2000.
- [51] X. Pan, C. Lin, H. Brody, and J. Morral, "An assessment of thermodynamic data for the liquid phase in the Al-rich corner of the Al-Cu-Si system and its application to the solidification of a 319 alloy," *Journal of phase equilibria and diffusion*, vol. 26, no. 3, pp. 225-233, 2005.

- [52] Z. Ma, E. Samuel, A. Mohamed, A. Samuel, F. Samuel, and H. Doty, "Influence of aging treatments and alloying additives on the hardness of Al–11Si–2.5 Cu–Mg alloys," *Materials & Design*, vol. 31, no. 8, pp. 3791-3803, 2010.
- [53] J. M. Boileau, C. A. Cloutier, L. A. Godlewski, P. A. Reeber-Symanski, C. Wolverton, and J. E. Allison, "The dimensional stability of cast 319 aluminum," *SAE transactions*, pp. 385-395, 2003.
- [54] F. Samuel, "Incipient melting of Al₁₅Mg₈Si₆Cu₂ and Al₂Cu intermetallics in unmodified and strontium-modified Al–Si–Cu–Mg (319) alloys during solution heat treatment," *Journal of Materials Science*, vol. 33, no. 9, pp. 2283-2297, 1998.
- [55] A. M. A. Mohamed, F. H. Samuel, and S. Al kahtani, "Influence of Mg and solution heat treatment on the occurrence of incipient melting in Al–Si–Cu–Mg cast alloys," *Materials Science and Engineering: A*, vol. 543, pp. 22-34, 2012/05/01/ 2012.
- [56] E. Sjölander and S. Seifeddine, "The heat treatment of Al–Si–Cu–Mg casting alloys," *Journal of materials processing technology*, vol. 210, no. 10, pp. 1249-1259, 2010.
- [57] S. Shivkumar, S. Ricci, C. Keller, and D. Apelian, "Effect of solution treatment parameters on tensile properties of cast aluminum alloys," *Journal of Heat Treating*, vol. 8, no. 1, pp. 63-70, 1990.
- [58] N. Crowell and S. Shivkumar, "Solution Treatment Effects in Cast Al-Si-Cu Alloys (95-107)," *Transactions of the American Foundrymen's Society*, vol. 103, pp. 721-726, 1995.
- [59] E. Sjölander and S. Seifeddine, "Optimization of solution treatment of cast Al-7Si-0.3 Mg and Al-8Si-3Cu-0.5 Mg alloys," *Metallurgical and Materials Transactions A*, vol. 45, no. 4, pp. 1916-1927, 2014.
- [60] J. H. Sokolowski *et al.*, "The removal of copper-phase segregation and the subsequent improvement in mechanical properties of cast 319 aluminium alloys by a two-stage solution heat treatment," *Journal of Materials Processing Technology*, vol. 53, no. 1-2, pp. 385-392, 1995.
- [61] J. H. Sokolowski, M. B. Djurdjevic, C. A. Kierkus, and D. O. Northwood, "Improvement of 319 aluminum alloy casting durability by high temperature solution treatment," *Journal of Materials Processing Technology*, vol. 109, no. 1-2, pp. 174-180, 2001.
- [62] G. Wang, X. Bian, W. Wang, and J. Zhang, "Influence of Cu and minor elements on solution treatment of Al–Si–Cu–Mg cast alloys," *Materials Letters*, vol. 57, no. 24, pp. 4083-4087, 2003/08/01/ 2003.
- [63] D. Zhang and L. Zheng, "The quench sensitivity of cast Al-7 wt pct Si-0.4 wt pct Mg alloy," *Metallurgical and Materials Transactions A*, vol. 27, no. 12, pp. 3983-3991, 1996.
- [64] S. Weakley-Bollin, W. Donlon, C. Wolverton, J. Allison, and J. Jones, "Modeling the age-hardening behavior of Al-Si-Cu alloys," *Metallurgical and materials transactions A*, vol. 35, no. 8, pp. 2407-2418, 2004.
- [65] A. Wiengmoon, J. T. Pearce, T. Chairuang斯里, S. Isoda, H. Saito, and H. Kurata, "HRTEM and HAADF-STEM of precipitates at peak ageing of cast A319 aluminium alloy," *Micron*, vol. 45, pp. 32-36, 2013.
- [66] L. Ratke and P. W. Voorhees, *Growth and coarsening: Ostwald ripening in material processing*. Springer Science & Business Media, 2002.
- [67] M. E. Fine, "Precipitation hardening of aluminum alloys," *Metallurgical Transactions A*, vol. 6, no. 4, pp. 625-630, 1975.

- [68] C. C. Engler-Pinto, J. V. Lasecki, J. M. Boileau, and J. E. Allison, "A comparative investigation on the high temperature fatigue of three cast aluminum alloys," SAE Technical Paper0148-7191, 2004.
- [69] D. Löhe, T. Beck, and K.-H. Lang, "Important aspects of cyclic deformation, damage and lifetime behaviour in thermomechanical fatigue of engineering alloys," 2004.
- [70] W. Zhuang and N. S. Swansson, "Thermo-mechanical fatigue life prediction: A critical review," 1998.
- [71] J. Jones, M. Whittaker, R. Lancaster, and S. Williams, "The influence of phase angle, strain range and peak cycle temperature on the TMF crack initiation behaviour and damage mechanisms of the nickel-based superalloy, RR1000," *International Journal of Fatigue*, vol. 98, pp. 279-285, 2017.
- [72] M. Riedler, H. Leitner, B. Prillhofer, G. Winter, and W. Eichlseder, "Lifetime simulation of thermo-mechanically loaded components," *Meccanica*, vol. 42, no. 1, pp. 47-59, 2007.
- [73] R. Minichmayr, M. Riedler, G. Winter, H. Leitner, and W. Eichlseder, "Thermo-mechanical fatigue life assessment of aluminium components using the damage rate model of Sehitoglu," *International Journal of Fatigue*, vol. 30, no. 2, pp. 298-304, 2008.
- [74] X. Su *et al.*, "Thermomechanical fatigue analysis of cast aluminum engine components," Dans *Thermomechanical Fatigue Behavior of Materials: 4th Volume*: ASTM International, 2003.
- [75] Y. Jang, S. Jin, Y. Jeong, and S. Kim, "Fatigue crack initiation mechanism for cast 319-T7 aluminum alloy," *Metallurgical and Materials Transactions A*, vol. 40, no. 7, pp. 1579-1587, 2009.
- [76] V. Firouzdor, M. Rajabi, E. Nejati, and F. Khomamizadeh, "Effect of microstructural constituents on the thermal fatigue life of A319 aluminum alloy," *Materials Science and Engineering: A*, vol. 454-455, pp. 528-535, 2007/04/25/ 2007.
- [77] R. Gundlach, B. Ross, A. Hetke, S. Valtierra, and J. Mojica, "Thermal Fatigue Resistance of Hypoeutectic Aluminum-Silicon Casting Alloys (94-141)," *Transactions of the American Foundrymen's Society*, vol. 102, pp. 205-224, 1994.
- [78] H. Sehitoglu, C. Engler-Pinto, H. Maier, and T. Foglesong, "Thermomechanical deformation of AL319 Alloys with different iron contents," *Proceedings CAMP2002–High Temperature Fatigue, S*, pp. 76-83, 2002.
- [79] P. Huter, P. Renhart, S. Oberfrank, M. Schwab, F. Grün, and B. Stauder, "High- and low-cycle fatigue influence of silicon, copper, strontium and iron on hypo-eutectic Al–Si–Cu and Al–Si–Mg cast alloys used in cylinder heads," *International Journal of Fatigue*, vol. 82, pp. 588-601, 2016/01/01/ 2016.
- [80] P. Huter, S. Oberfrank, F. Grün, and B. Stauder, "Thermo-mechanical fatigue influence of copper and silicon on hypo-eutectic Al–Si–Cu and Al–Si–Mg cast alloys used in cylinder heads," *International Journal of Fatigue*, vol. 88, pp. 142-155, 2016/07/01/ 2016.
- [81] K. Moizumi, H. Tezuka, and T. Sato, "Influence of Cu and Mg addition on mechanical properties and thermal fatigue life of Al-Si-Mg cast alloys for cylinder head," *Journal of Japan Foundry Engineering Society*, vol. 75, no. 6, pp. 397-402, 2003.
- [82] K. MOIZUMI, H. TEZUKA, and T. SATO, "Influence of precipitation hardening and eutectic Si microstructures on thermal fatigue life of Al-Si-Mg-Cu based cast alloys," *Keikinzoku*, vol. 54, no. 6, pp. 205-210, 2004.

- [83] P. Shower, S. Roy, C. S. Hawkins, and A. Shyam, "The effects of microstructural stability on the compressive response of two cast aluminum alloys up to 300°C," *Materials Science and Engineering: A*, vol. 700, pp. 519-529, 2017/07/17/ 2017.
- [84] S. Roy, L. F. Allard Jr, A. Rodriguez, W. D. Porter, and A. Shyam, "Comparative evaluation of cast aluminum alloys for automotive cylinder heads: Part II: Mechanical and thermal properties," *Metallurgical and Materials Transactions. A, Physical Metallurgy and Materials Science*, vol. 48, no. 5, 2017.
- [85] P. Shower, J. R. Morris, D. Shin, B. Radhakrishnan, L. F. Allard, and A. Shyam, "Temperature-dependent stability of θ' -Al₂Cu precipitates investigated with phase field simulations and experiments," *Materialia*, vol. 5, p. 100185, 2019/03/01/ 2019.
- [86] H. Sehitoglu, T. Smith, X. Qing, H. J. Maier, and J. Allison, "Stress-strain response of a cast 319-T6 aluminum under thermomechanical loading," *Metallurgical and Materials Transactions A*, vol. 31, no. 1, pp. 139-151, 2000.
- [87] Q. Wang, D. Apelian, and D. Lados, "Fatigue behavior of A356-T6 aluminum cast alloys. Part I. Effect of casting defects," *Journal of light metals*, vol. 1, no. 1, pp. 73-84, 2001.
- [88] K. Moizumi, K. Mine, H. Tezuka, and T. Sato, "Influence of precipitate microstructures on thermal fatigue properties of Al-Si-Mg cast alloys," *Dans Materials Science Forum*, 2002, vol. 396, pp. 1371-1376: Trans Tech Publ.
- [89] J. J. Moverare, "Thermal–mechanical fatigue behaviour of CMSX-4 in virgin and long term aged conditions," *Materials Science and Technology*, vol. 23, no. 12, pp. 1450-1453, 2007/12/01 2007.
- [90] K. S. Chan, P. Jones, and Q. Wang, "Fatigue crack growth and fracture paths in sand cast B319 and A356 aluminum alloys," *Materials science and Engineering: A*, vol. 341, no. 1-2, pp. 18-34, 2003.
- [91] M. Azadi and M. M. Shirazabad, "Heat treatment effect on thermo-mechanical fatigue and low cycle fatigue behaviors of A356.0 aluminum alloy," *Materials & Design*, vol. 45, pp. 279-285, 2013/03/01/ 2013.
- [92] S. Nandy, A. P. Sekhar, T. Kar, K. K. Ray, and D. Das, "Influence of ageing on the low cycle fatigue behaviour of an Al–Mg–Si alloy," *Philosophical Magazine*, vol. 97, no. 23, pp. 1978-2003, 2017/08/13 2017.
- [93] M. Toyoda, H. Toda, H. Ikuno, T. Kobayashi, M. Kobayashi, and K. Matsuda, "Preferential orientation of precipitates during thermomechanical cyclic loading in an aluminum alloy," *Scripta materialia*, vol. 56, no. 5, pp. 377-380, 2007.
- [94] H. Toda, T. Fukunaga, and M. Kobayashi, "Improvement of thermomechanical fatigue life in an age-hardened aluminum alloy," *Scripta Materialia*, vol. 60, no. 6, pp. 385-387, 2009.
- [95] T. Beck, D. Löhé, J. Luft, and I. Henne, "Damage mechanisms of cast Al–Si–Mg alloys under superimposed thermal–mechanical fatigue and high-cycle fatigue loading," *Materials Science and Engineering: A*, vol. 468, pp. 184-192, 2007.
- [96] T. Beck, I. Henne, and D. Löhé, "Lifetime of cast AlSi6Cu4 under superimposed thermal–mechanical fatigue and high-cycle fatigue loading," *Materials Science and Engineering: A*, vol. 483, pp. 382-386, 2008.
- [97] S. S. Manson, *Behavior of materials under conditions of thermal stress*. National Advisory Committee for Aeronautics, 1953.
- [98] M. Miller, D. McDowell, and R. Oehmke, "A creep-fatigue-oxidation microcrack propagation model for thermomechanical fatigue," 1992.

- [99] N. Dowling and J. Begley, "Fatigue crack growth during gross plasticity and the J-integral," Dans *Mechanics of crack growth*: ASTM International, 1976.
- [100] M. Okazaki and T. Koizumi, "Crack propagation of steels during low cycle thermal-mechanical and isothermal fatigue at elevated temperatures," *Metallurgical Transactions A*, vol. 14, no. 8, pp. 1641-1648, 1983.
- [101] T. Takahashi, A. Koike, and K. Sasaki, "Inelastic behavior and low cycle fatigue of aluminum alloy subjected to thermo-mechanical loading," *SAE transactions*, pp. 454-461, 1998.
- [102] T. J. Smith, H. Sehitoglu, E. Fleury, H. J. Maier, and J. Allison, "Modeling high-temperature stress-strain behavior of cast aluminum alloys," *Metallurgical and Materials Transactions A*, vol. 30, no. 1, pp. 133-146, 1999.
- [103] R. Skelton, "Energy criterion for high temperature low cycle fatigue failure," *Materials science and technology*, vol. 7, no. 5, pp. 427-440, 1991.
- [104] W. Ostergren, "A damage function and associated failure equations for predicting hold time and frequency effects in elevated temperature, low cycle fatigue," *Journal of Testing and Evaluation*, vol. 4, no. 5, pp. 327-339, 1976.
- [105] T. Gocmez, A. Awarke, and S. Pischinger, "A new low cycle fatigue criterion for isothermal and out-of-phase thermomechanical loading," *International Journal of Fatigue*, vol. 32, no. 4, pp. 769-779, 2010.
- [106] Y.-N. Fan, H.-J. Shi, and K. Tokuda, "A generalized hysteresis energy method for fatigue and creep-fatigue life prediction of 316L (N)," *Materials Science and Engineering: A*, vol. 625, pp. 205-212, 2015.
- [107] M. Wang, J. Pang, M. Zhang, H. Liu, S. Li, and Z. Zhang, "Thermo-mechanical fatigue behavior and life prediction of the Al-Si piston alloy," *Materials Science and Engineering: A*, vol. 715, pp. 62-72, 2018.
- [108] M. Wang, J. Pang, H. Liu, S. Li, M. Zhang, and Z. Zhang, "Effect of constraint factor on the thermo-mechanical fatigue behavior of an Al-Si eutectic alloy," *Materials Science and Engineering: A*, vol. 783, p. 139279, 2020.
- [109] P. Hähner, E. Affeldt, T. Beck, H. Klingelhöffer, M. Loveday, and C. Rinaldi, "Validated code-of-practice for strain-controlled thermo-mechanical fatigue testing," *Institute for Energy, Petten*, 2006.
- [110] *ASTM E2368-10, Standard Practice for Strain Controlled Thermomechanical Fatigue Testing*, 2010.
- [111] *ASTM E606 / E606M-21, Standard Test Method for Strain-Controlled Fatigue Testing*, 2021.
- [112] J. Qin, D. Racine, K. Liu, and X. Chen, "Strain-controlled thermo-mechanical fatigue testing of aluminum alloys using the Gleeble 3800 system," Dans *International Aluminum Alloys Conference (ICAA16)*, 2018.
- [113] S. Chen, K. Liu, and X.-G. Chen, "Elevated-Temperature Low-Cycle Fatigue Behaviors of Al-Si 356 and 319 Foundry Alloys," Cham, 2019, pp. 251-257: Springer International Publishing.
- [114] A. Baldan, "Review progress in Ostwald ripening theories and their applications to nickel-base superalloys Part I: Ostwald ripening theories," *Journal of materials science*, vol. 37, no. 11, pp. 2171-2202, 2002.
- [115] I. Lifshitz and V. Slezov, "Kinetics of diffusive decomposition of supersaturated solid solutions," *Soviet Physics JETP*, vol. 35, no. 8, pp. 331-339, 1959.

- [116] C. Kuehmann and P. Voorhees, "Ostwald ripening in ternary alloys," *Metallurgical and Materials Transactions A*, vol. 27, no. 4, pp. 937-943, 1996.
- [117] T. Philippe and P. W. Voorhees, "Ostwald ripening in multicomponent alloys," *Acta Materialia*, vol. 61, no. 11, pp. 4237-4244, 2013/06/01/ 2013.
- [118] J. Tiley, G. B. Viswanathan, R. Srinivasan, R. Banerjee, D. M. Dimiduk, and H. L. Fraser, "Coarsening kinetics of γ' precipitates in the commercial nickel base Superalloy René 88 DT," *Acta Materialia*, vol. 57, no. 8, pp. 2538-2549, 2009/05/01/ 2009.
- [119] A. J. Ardell and V. Ozolins, "Trans-interface diffusion-controlled coarsening," *Nature Materials*, vol. 4, no. 4, pp. 309-316, 2005/04/01 2005.
- [120] G. Liu, G. J. Zhang, X. D. Ding, J. Sun, and K. H. Chen, "Modeling the strengthening response to aging process of heat-treatable aluminum alloys containing plate/disc- or rod/needle-shaped precipitates," *Materials Science and Engineering: A*, vol. 344, no. 1, pp. 113-124, 2003/03/15/ 2003.
- [121] Y. H. Chen and R. D. Doherty, "On the growth kinetics of plate-shaped precipitates in aluminium-copper and aluminium-gold alloys," *Scripta Metallurgica*, vol. 11, no. 9, pp. 725-729, 1977/09/01/ 1977.
- [122] R. Sankaran and C. Laird, "Further comments on the kinetics of growth of plate precipitates in Al - Ag, Al - Au and Al - Cu alloys," *Scripta Metallurgica*, vol. 12, no. 10, pp. 877-883, 1978/10/01/ 1978.
- [123] M. Wang, J. Pang, H. Liu, C. Zou, S. Li, and Z. Zhang, "Deformation mechanism and fatigue life of an Al-12Si alloy at different temperatures and strain rates," *International Journal of Fatigue*, vol. 127, pp. 268-274, 2019.
- [124] L. Tian *et al.*, "Elevated re-aging of a piston aluminium alloy and effect on the microstructure and mechanical properties," *Materials Science and Engineering: A*, vol. 738, pp. 375-379, 2018.
- [125] M. Lin, G. Gottstein, and L. Shvindlerman, "Generalized Gibbs-Thomson equation for nanoparticles at grain boundaries," *Acta Materialia*, vol. 129, pp. 361-365, 2017.
- [126] A. Richter, C.-L. Chen, R. Smith, E. McGee, R. Thomson, and S. Kenny, "Hot stage nanoindentation in multi-component Al-Ni-Si alloys: Experiment and simulation," *Materials Science and Engineering: A*, vol. 494, no. 1-2, pp. 367-379, 2008.
- [127] R. Liu, Z. Zhang, P. Zhang, and Z. Zhang, "Extremely-low-cycle fatigue behaviors of Cu and Cu-Al alloys: Damage mechanisms and life prediction," *Acta Materialia*, vol. 83, pp. 341-356, 2015.
- [128] C. Shao, P. Zhang, R. Liu, Z. Zhang, J. Pang, and Z. Zhang, "Low-cycle and extremely-low-cycle fatigue behaviors of high-Mn austenitic TRIP/TWIP alloys: property evaluation, damage mechanisms and life prediction," *Acta Materialia*, vol. 103, pp. 781-795, 2016.